July 2017

Novel Transducer Calibration and Simulation Verification of Polydimethylsiloxane (PDMS) Channels on Acoustic Microfluidic Devices

Scott T. Padilla
University of South Florida, spadill2@mail.usf.edu

Novel Transducer Calibration and Simulation Verification of Polydimethylsiloxane

(PDMS) Channels on Acoustic Microfluidic Devices

by

Scott T. Padilla

A dissertation submitted in partial fulfillment
of the requirements for the degree of
Doctor of Philosophy
Department of Mechanical Engineering
College of Engineering
University of South Florida

Major Professor: Rasim Guldiken, Ph.D.
Nathan Crane, Ph.D.
David Eddins, Ph.D.
Jose Porteiro, Ph.D.
Jing Wang, Ph.D.

Date of Approval:
June 20, 2017

Keywords: Ultrasonic Bone Conduction, Piezoelectricity, Insertion Loss, Finite Element Analysis, Surface Acoustic Waves

DEDICATION

I would like to dedicate this work to everyone who has been there to support me. To my parents, Pamela and Antonio, who gave me the opportunity to pursue my Ph.D., and to my sisters, Meli and Pami, who have been my role models my entire life. To my girlfriend, Leah, who has spent countless late nights keeping me company and was always there to proofread my poor grammar, and finally, to all of my friends. Without each one of you, this would have not been possible.

ACKNOWLEDGMENTS

I would like to acknowledge a few key people who have been pivotal during my time as a graduate student, and more particularly during the pursuit of my doctorate.

Dr. Rasim Guldiken, my major advisor. Since I started in your lab group, you have always been around to guide my studies and you have provided me with numerous opportunities to further my academic growth. I will always be grateful for the many hours you have spent with me over the years, and I know that I would not have been able to reach this point without your support. I sincerely hope that this is not the last time I will be able to work with you, as this process has been not only vastly educating to me, but enjoyable as well.

Dr. Jose Porteiro, one of my committee advisors. When I was completing my undergraduate studies, I was considering graduate school, but I was not sure if it would be the right fit for me. After I received my B.S. however, you took the time to talk to me about what would be involved in pursuing a graduate degree, and you gave me the confidence to apply for the Ph.D. program. You have also spent more time than was required, and kept me motivated during the process, thank you.

Dr. David Eddins, Dr. Jing Wang, and Dr. Nathan Crane, my committee members, and Dr. Andrés E. Tejada-Martinéz, my committee chair. Each of you have spent time meeting with me and discussing my projects over my time as a graduate student. I would not have learned nearly as much as I have during this process if it wasn't for your expertise, time, and dedication to the students at USF.

I would also like to acknowledge my lab members and other students, who after getting to know them over the years I now consider my friends. Dr. Tao Wang, Dr Emre Tufekcioglu, Senmiao Hu, Joel Cooper, Adrian Avila, and Carl Schousboe. I did not know any of you when I started this program, but I know my experience would not have been the same without each of you.

Finally, I would like to acknowledge my parents, Pamela Padilla and Antonio Padilla. For as long as I can remember you have always pushed me to be the best student I can be. You made me work harder and achieve more than I ever thought I could, and there is no doubt that the work I have completed, not only during my graduate studies, but over my entire life, is as much your accomplishment as it is mine.

TABLE OF CONTENTS

LIST OF TABLES

LIST OF FIGURES

ABSTRACT

The work and results presented in this dissertation concern two complimentary studies that are rooted in surface acoustic waves and transducer study.

Surface acoustic wave devices are utilized in a variety of fields that span biomedical applications to radio wave transmitters and receivers. Of interest in this dissertation is the study of surface acoustic wave interaction with polydimethylsiloxane. This material, commonly known as PDMS, is widely used in the microfluidic field applications in order to create channels for fluid flow on the surface of a piezoelectric substrate. The size, and type of PDMS that is created and ultimately etched on the surface of the substrate, plays a significant role in its operation, chiefly in the insertion loss levels experienced. Here, through finite element analysis, via ANSYS® 15 Finite Element Modeling software, the insertion loss levels of varying PDMS sidewall channel dimensions, from two to eight millimeters is investigated. The simulation is modeled after previously published experimental data, and the results demonstrate a clear increase in insertion loss levels with an increase in channel sidewall dimensions. Analysis of the results further show that due to the viscoelastic nature of PDMS, there is a non -linear increase of insertion loss as the sidewall dimensions thicken. There is a calculated variation of 8.31 decibels between the insertion loss created in a microfluidic device with a PDMS channel sidewall thickness of eight millimeters verse a thickness of two millimeters. Finally, examination of the results show that insertion loss levels in a device are optimized when the PDMS sidewall channels are between two and four millimeters.

The second portion of this dissertation concerns the calibration of an ultrasonic transducer. This work is inspired by the need to properly quantify the signal generated by an ultrasonic transducer, placed under a static loading condition, that will be used in measuring ultrasonic bone conducted frequency perception of human subjects. Ultrasonic perception, classified as perception beyond the typical hearing limit of approximately 20 kHz, is a subject of great interest in audiology. Among other reasons, ultrasonic signal perception in humans is of interest because the mechanism by which either the brain or the ear interprets these signals is not entirely understood. Previous studies have utilized ultrasonic transducers in order to study this ultrasonic perception; however, the calibration methods taken, were either incomplete or did not properly account for the operation conditions of the transducers. A novel transducer calibration method is detailed in this dissertation that resolves this issue and provides a reliable means by which the signal that is being created can be compared to the perception of human subjects.

CHAPTER 1. INTRODUCTION

The main objectives of this dissertation are to create an in-depth simulation study of surface acoustic wave (SAWs) transducers integrated with microfluidic channels, and the creation of a novel technique for the calibration of preloaded acoustic transducers.

Surface acoustic waves are mechanical wave motions which are generated on, and propagate elastically on, the surface of a substrate or medium. The energy of these mechanical waves declines exponentially as they penetrate into the depth of the substrate they are propagating on; this is characterized by a loss in wave amplitude. SAWs find their roots in the discovery of Rayleigh waves by British physicist Lord Rayleigh, John William Strut, through his mathematical theory of Rayleigh Scattering [1]. After their discovery, SAWs found many fields of application such as non-destructive testing, through the investigation of faults in a materials surface, biochemical sensors, and Radio Frequency communications. More recently, SAWs have found an increase in application in the field of microfluidics, this is due to two primary reasons. First, energy from SAW waves is efficiently transferred into the bulk of a liquid placed in contact with them. Second, SAWs create larger magnitude of force transfer than other methods in the microfluidic field such as magnetism, electrowetting, and thermo capillarity[2]. In this dissertation, SAWs are simulated on a lithium niobate, $LiNbO_3$, substrate by taking advantage of the piezoelectric effect.

The piezoelectric effect is the creation of an electrical charge in certain materials when they are subjected to mechanical stress. One of the most unique aspects of the piezoelectric effect is that it is completely reversible. When the same material is subjected to an electric charge, the

material will undergo a mechanical stress. This effect is caused by the manipulation of the atomic structure of piezo electric materials. In their unaltered state, piezoelectric materials have very finely internally balance charges in their crystalline structure [3]. When a voltage is induced into a piezo electric material, an electrical pressure is induced on the structure of the material, which will rearrange its internal structure to balance the charges. When the voltage is removed, the crystal then returns to its unaltered state. This effect is utilized in order to easily and repeatedly create surface acoustic waves in microfluidic devices, through the use of interdigital transducers, IDTs. These IDTs have comb shaped interlocking fingers, and are used in sets of two. The first set of the IDTs are used for the input; this set is responsible for transmitting any electric voltage into a piezoelectric substance to create SAWs. The second set of IDTs, the "receiver" set, is responsible for reading how much voltage is created in the piezoelectric devices [4]. The ratio of this input to output voltage is used to calculate the insertion loss of a device. The insertion loss is important for finding the fundamental frequency of the device being used, which defines the optimal operating frequency [5]. This dissertation contains a simulation study that details how the insertion loss of a device is effected by altering elements of its design.

The second focus of this dissertation contains a novel method for calibration of an ultrasonic transducer that is placed under a static load. Currently a large industry exists which focuses on calibration of transducers for general use; however, for specialized transducer operating characteristics there is not always a readily available option. Furthermore, for the specific use of ultrasonic bone conduction, there does not exist an accurate method of transducer calibration. Calibration of any signal producing device is a key component for both properly characterizing a signal being created, and analyzing its effects. The method detailed in this dissertation centers on identifying the signal output of an ultrasonic transducer operating between 20 kHz to 80 kHz.

1.1 Motivation

As computer processing power increases, the capabilities of computer simulation accuracy and detail rise alongside it [6]. This makes simulation a very feasible alternative to actual fabrication and experimentation of microfluidic devices in instances where time, budget, or even capability of fabrication of a device are constrained. A further advantage of simulation is that it affords a user the ability to make small adjustments in their designs to optimize a device before its fabrication. Time will always be a constraint, even in cases where budget would not be considered an issue for realizing devices. This dissertation will detail the steps utilized in creating an in depth and accurate simulation of the insertion loss of a microfluidic device. Furthermore, these simulation results will be compared to published experimental data.

The motivation behind the second focus of this dissertation is the need for an accurate calibration method for a transducer that will be used for ultrasonic bone conduction. Ultrasonic bone conduction is an application that has been studied in audiology as far back as 1963 [7]. Calibration for this type of application is extremely important, as it is intended to be used as a reference for testing with patient participants. Although the methods for calibration described in this dissertation were created for an ultrasonic bone conductor, they can be utilized in other specialized situations where more traditional calibration methods are not available.

1.2 Dissertation Organization

This dissertation is organized in the following manner.

Chapter 2 contains a theoretical background that will lay the basis for work completed. The theoretical background will focus on the fundamental working principles of surface acoustic waves, insertion loss, and piezoelectricity. After establishing this background, this chapter will

cover in detail important aspects of simulation, including: meshing, material properties, boundary conditions, and actuating loads.

Chapter 3 will discuss the previous work that has been done in ultrasonic bone calibration. This will establish a clear reason for the necessity of a new method to accurately calibrate bone conducting transducers. This chapter will also discuss the biomechanics of the hearing process.

Chapter 4 will contain the novel calibration method used in this dissertation. In specific, it will cover: the transducers that were selected for initial testing, the equipment used in the calibration procedure, and the calibration rig created for the testing procedure.

Chapter 5 will detail the specifics chosen for each aspect of the simulation completed for this dissertation. The simulation focuses on insertion loss variation caused by varying PDMS channel dimensions bonded on top of a piezoelectric substrate, lithium niobate, $LiNbO_3$ in this study, and a comparison with previously published experimental results.

Finally, chapter 6 is a discussion of future work that can be completed from this dissertation. It will specify areas of the simulation that can be further studied in detail. This chapter will also contain ideas on how the calibration methods for ultrasonic preloaded transducers can still be improved.

CHAPTER 2. SAW THEORY AND FINITE ELEMENT ANALYSIS

2.1 Piezoelectric Effect

Piezoelectricity was discovered by the Curie brothers in 1880 through their demonstration that quartz could generate a charge when mechanically deformed [3]. This effect of creating an electrical charge on a crystalline structure by subjecting it to a mechanical deformation is known as the piezoelectric effect. Conversely the piezoelectric effect causes crystalline materials to undergo a deformation when subjected to a voltage. Not all crystals are piezoelectric, only materials that are non-centrosymmetric can exhibit the piezoelectric effect [8]. Non-centrosymmetric crystals have no inversion center point in their structure, which causes them to have anisotropic material and electrical properties [9]. Figure 2.1 Piezoelectric Effect Diagram provides a depiction of what causes the piezoelectric effect in non-centrosymmetric crystals.

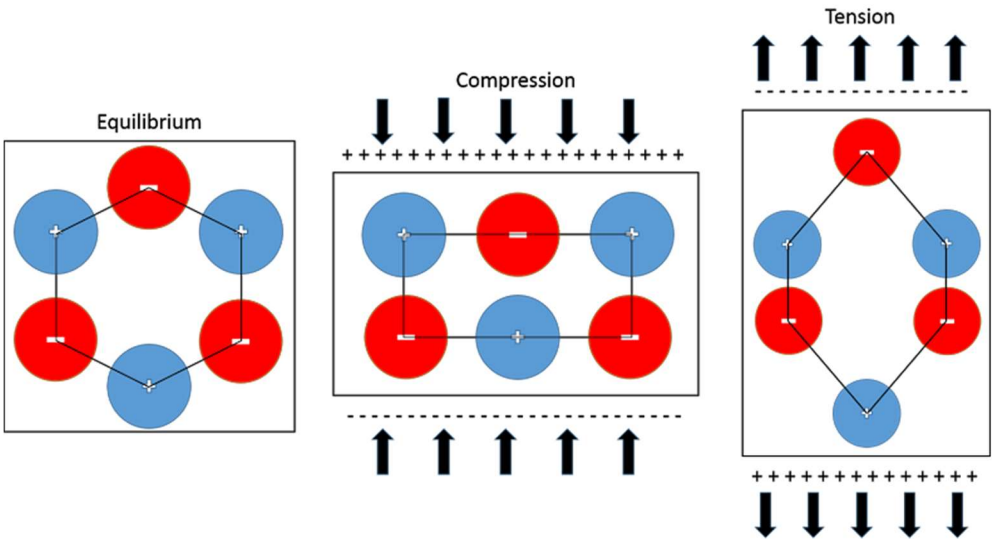

Figure 2.1 Piezoelectric Effect Diagram

Figure 2.1 Piezoelectric Effect Diagram illustrates that while under no stress, the positively and negatively charged atoms of the structure are balanced; however, when placed under deformation the structure is polarized. In the tension case, positive atoms are moved close to the material's top surface creating a positive charge, and negative atoms are moved towards the material's bottom surface which creates a negative charge. The opposite polarization is created in the material when it is placed under compression. This figure also helps to demonstrate that piezoelectric materials are typically crystals with ionic bonds [8].

2.2 Piezoelectric Mathematical Background

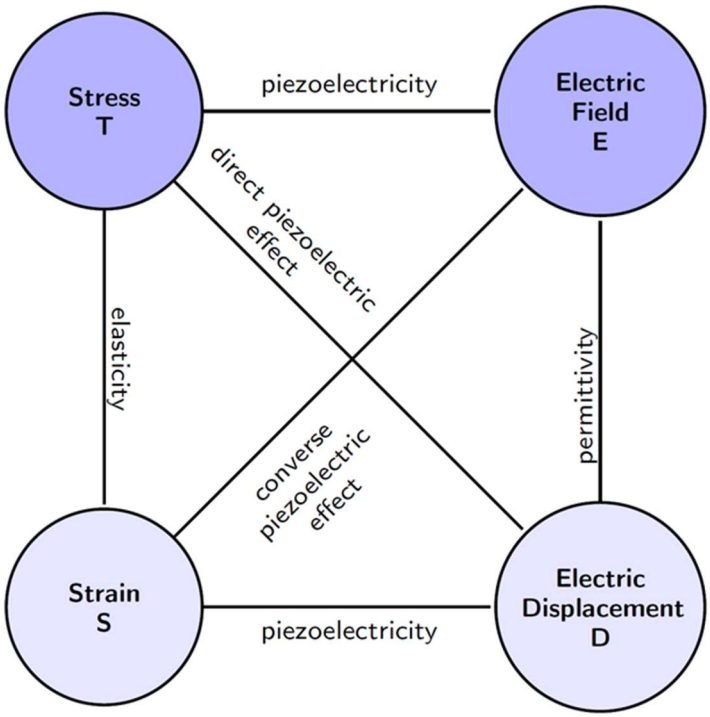

Figure 2.2 Partial Heckmann Diagram

The partial Heckmann diagram in Figure 2.2 illustrates the relationship between mechanical and electrical properties of piezoelectric materials. The two types of piezoelectric effects are labeled as the direct piezo electric effect, and the converse piezoelectric effect. The direct piezoelectric effect is defined by the relationship between mechanical stress and electrical

polarization of the material, and the converse piezoelectric effect is defined by the relationship between mechanical strain and an applied electrical field [10]. The equations of both types of the piezoelectric effect are related through the principle piezoelectric coefficient, *d*. These equations are as follows [10].

$$P = dX \tag{1}$$

$$x = dE \tag{2}$$

In the direct piezoelectric effect equation, (1), *P* accounts for the polarization and *X* accounts for the stress. In the indirect piezoelectric effect equation, (2), *x* accounts for the strain and *E* accounts for the electric field. Since piezoelectric materials are non-centrosymmetric, these equations only describe the general effects, and are transformed into (3) and (4), below, to account for their anisotropy.

$$P_j = d_{ijk}X_{ik} \tag{3}$$

$$x_{ij} = d_{ijk}E_k \tag{4}$$

In these equations, polarization (*P*) and electrical field are vectors (*E*), stress (*X*) and strain (*x*) are second rank tensors, and the piezoelectric coefficient (*d*) is a third rank tensor [10].

Equations (3) and (4) apply to special cases where only stress and strain are present. In order to account for the effects of piezoelectricity on a structure, (5)and (6) for stress and strain in non-piezoelectric structures are introduced.

$$\sigma_i = C_{ij}\varepsilon_j \tag{5}$$

$$\varepsilon_i = S_{ij}\sigma_j \tag{6}$$

In these equations, *C* represents the inverse stiffness matrix and *S* represents the compliance matrix. Combining these equations with (3) and (4) for piezoelectric structures, yields the equations (7) and (8), as seen below.

$$\varepsilon_i = S^E \sigma_j + d_{ijk} E_j \tag{7}$$

$$\sigma_i = C^E \varepsilon_j - e_{ijk} E_j \tag{8}$$

These are the most common representation of the piezoelectric equations. The variables d_{ijk} and e_{ijk} are different for each piezoelectric material and cut orientation. Specifics of the piezoelectric material studied in this dissertation, lithium niobate, and its cut orientation are discussed later in this dissertation.

2.3 Surface Acoustic Waves

Acoustic waves in solids are the result of the superposition of elastic particle movement [11]. In this dissertation, the type of waves that are studied are surface acoustic waves, also known as SAWs. In large part, surface acoustic waves are separated into longitudinal waves and shear waves. Figure 2.3 below displays a two-dimensional representation of these two types of waves.

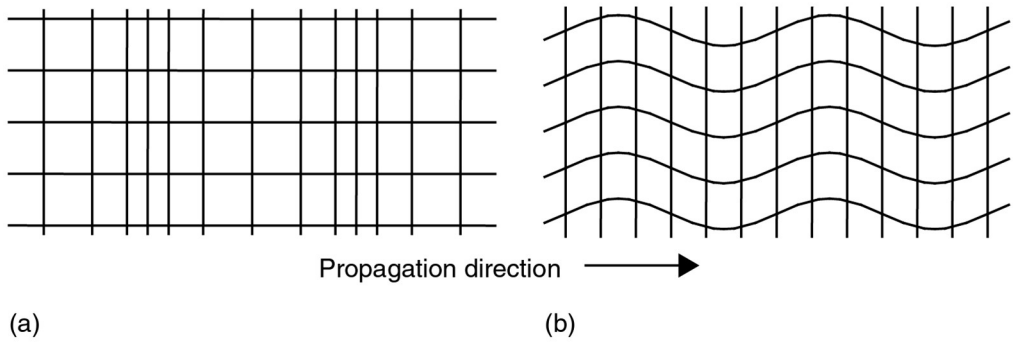

Figure 2.3 Two-Dimensional Representation of Longitudinal and Shear Waves

In Figure 2.3 Two-Dimensional Representation of Longitudinal and Shear Waves, nodal points at the intersection of horizontal and vertical lines in the grid represent individual particle positions. Figure 2.3 (a) depicts longitudinal wave movement. The nodal points oscillate from left to right with the propagation direction of the surface waves. Figure 2.3 (b) depicts shear wave action. The wave propagates from left to right, the same direction as the longitudinal wave;

however, the individual particles move up and down, in the normal direction of the wave's propagation.

The apparent wave motion created in these two classes of waves is the result of individual particle motion. When the superposition of particle motion is observed, this creates a visual effect of longitudinal and shear wave propagation. These two basic particle motions are combined in waves to create many different types of SAWs. Two of the most common types are Rayleigh waves and Love waves. These waves are distinguished from one another by their particle movement in relation to wave propagation direction [12]. They are depicted in Figure 2.4.

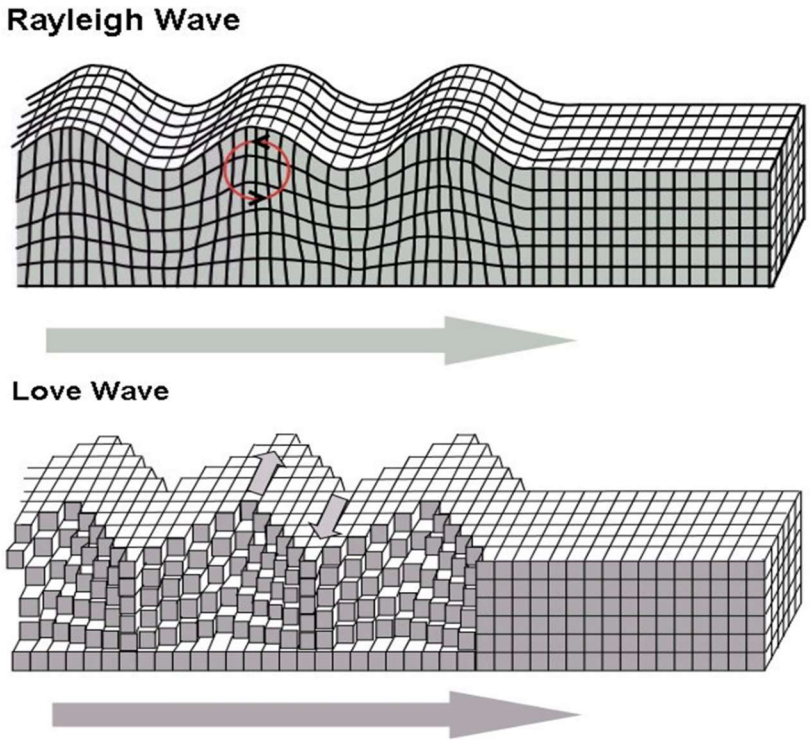

Figure 2.4 Three Dimensional SAW Waves (from [13, 14], public domain images)

The Love wave shown in Figure 2.4 is the result of the interaction of a multitude of pure shear type particle movements, while the Rayleigh wave shown is caused by the interaction of shear and longitudinal particle motions.

Pure shear waves present key advantages over Rayleigh waves in microfluidic applications. Rayleigh waves experience a higher level of attenuation when they travel across the sensing surface of a device. This is caused by energy loss when the wave penetrates into a fluid that is placed into contact with the substrate [15]. Alternatively, shear waves move normal to the surface of a fluid. This causes lower attenuation across the surface of a piezo electric substrate, and makes shear waves ideal for the type of microfluidic application that is studied.

2.4 Microfluidic Device Design

Microfluidic devices utilize the properties of surface acoustic waves through the use of interdigital transducers, commonly abbreviated as IDTs. The concept of using IDTs to both create and detect SAW signals was first proposed by R.M. White and F.W. Voltmer in 1965 [16]. Before the use of IDTs was a common practice, shear or compressive transducers were coupled to the face of the piezoelectric substrate to create waves. IDTs differ in that they are conductive material that is deposited directly onto the surface of a piezo electric substrate.

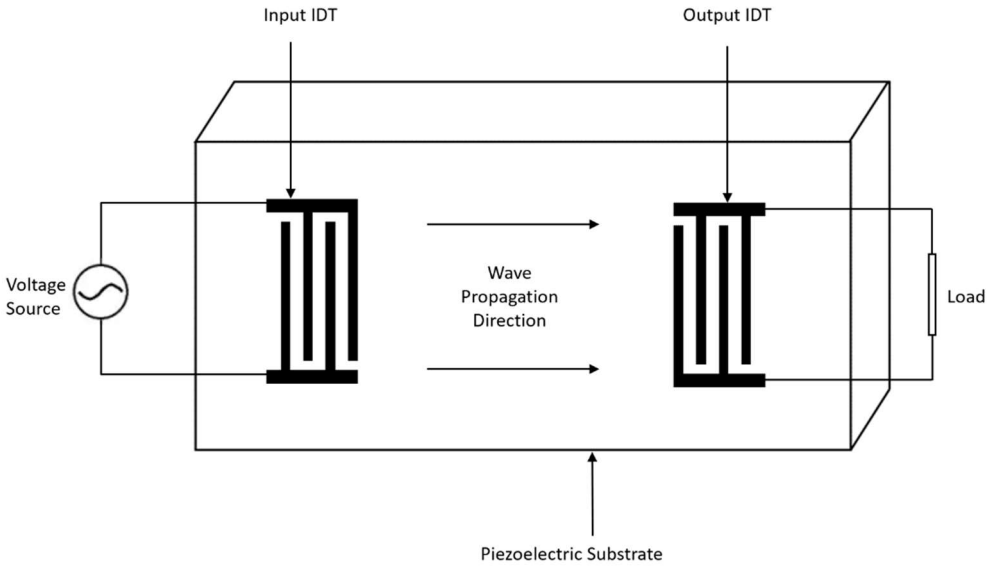

Figure 2.5 Basic SAW Device Components

Figure 2.5 is a depiction of a typical SAW device. The elements involved in this device are the piezo electric substrate, the input IDT, and the output IDT, both are deposited on top of the substrate. The substrate between the input and output IDTs can be used as a sensor surface or for actuating motion in a fluid. A voltage is applied to the input IDT, which subsequently creates a mechanical strain on the piezoelectric substrate via the piezoelectric effect. IDTs can be made of different types of metals; however, in this dissertation chrome IDTs are used [17]. Pulsing a voltage to the input IDTs creates waves that travel across the surface of the substrate. When the waves reach the set of output IDTs, the electrical charge created by their motion is converted back to a voltage. The amount of electrical energy that is converted to mechanical energy is calculated using the electromechanical coupling coefficient k_t which is given by:

$$k = \frac{d}{\sqrt{s^E \varepsilon^T}} \tag{9}$$

where d is the piezoelectric strain coefficient, s is the material compliance, and ε is the dielectric coefficient. These properties vary as a function of the piezoelectric substrate utilized.

The acoustic wavelength of a SAW device is a function of the spacing between two consecutive IDT fingers. The spacing between two fingers on opposite busses is equal to ¼ of the desired wavelength, λ. The spacing between two fingers of one bus is equal to one wavelength. In order to achieve this spacing, finger widths are also kept as one quarter of the desired operation. The operating frequency is calculated by equation (10),

$$f = \frac{V_{substrate}}{\lambda} \tag{10}$$

where f is the frequency calculated, $V_{substrate}$ is the velocity of propagation of waves through a given piezoelectric substrate, and λ is the wavelength chosen by IDT spacing. Since piezoelectric

materials have anisotropic properties, their operational propagation velocity is also effected by their crystal cut orientation.

SAW devices are furthermore dependent on the thickness of the IDT deposited on their surface. Thicker IDT fingers offer an excellent electrical contact with lower resistance, while thinner IDT fingers cause large circuit loading and insertion loss because of the higher resistances. If the IDT fingers are too thick; however, the impedance of transmission of acoustic waves increases, resulting in a reduction of the operating frequency due to a decrease in SAW velocity as the wave passes under the IDT fingers [18]. An IDT thickness of deposited metal of 500–2000 angstroms is ideal.[19]

Acoustic aperture is defined as the length of overlap of the interlocking fingers. Longer acoustic apertures in relation to acoustic wavelength lead to more focused wave travel. The minimum length of acoustic aperture that ensures uniform wave front travelling across a piezoelectric substrate is 30 times the designed wavelength.[20]

2.5 Finite Element Analysis

The number of factors that affect the operation of a microfluidic devices, as discussed in chapter 2.4, make their design and fabrication a costly and time expensive endeavor. In this dissertation, Finite Element Analysis (FEA) was used in the optimization of the microfluidic devices, using a commercially available software, ANSYS®.

Finite element analysis is a substantial and growing industry. In the United States alone, over one billion dollars is spent each year purchasing FEA software and the computer processing necessary to run it [21]. One of the applications of finite element analysis is the utilization of numerical method techniques to calculate the response of a complicated geometry to a stimulus [22]. These complicated geometries are broken down into a number of finite elements which

connect with each other through nodes [21]. There are several processes that are crucial in FEA for determining the accuracy and reliability of calculated results such as meshing, time discretization, and analysis method [23].

Key components in creating an ideal mesh for a finite element model are mesh density and mesh element type. The accuracy of solution increases with mesh density; however, too high mesh density has disadvantages. First, high mesh density greatly increases computational time, especially a transient analysis, where each mesh element node is calculated for each time step. Second, increases in mesh density have diminishing returns in solution accuracy, particularly if computation time is considered. Third, high mesh densities can artificially create stress singularities at points of stress concentration. As a mesh is refined near stress concentration points, the area of each individual element becomes smaller, artificially increasing the stress calculated [22]. For acoustic simulations, the recommended number of elements per wavelength is between six and ten [24].

A second factor in defining an ideal mesh is choosing the correct element type for a given finite element model. There are one-dimensional, two-dimensional, and three-dimensional element types; however, here only three-dimensional mesh elements are utilized. The two main subcategories of three-dimensional meshing use tetrahedral and/or hexahedral elements. Standard tetrahedral elements have four node points and standard hexahedral elements have eight node points, one at each element vertex. We use mostly hexahedral elements because they are easier to modify than tetrahedral elements; furthermore, in simple geometries, hexahedral elements allow for consistent meshing throughout a model [25].

In FEA, mesh quality is further analyzed through mesh quality metrics. Element quality, aspect ratio, skewness, and orthogonal quality are major metrics that help determine whether a

generated mesh is suitable for computational analysis. Element quality for three dimensional elements is calculated through:

$$Element\ Quality = C\left(\frac{Volume}{\sqrt{[\sum edge\ length^2]^3}}\right) \tag{11}$$

where *C* is a constant that depends on the type of element used. These values are found in Table 2.1. The element quality calculation helps determine the variation of an element from its ideal equilateral shape. In calculating element quality, the volume a created three-dimensional mesh element is compared to the sum of its edge sizes and given as a dimensionless value.

Table 2.1 Values of *C* for Element Quality Calculation [26]

Element	**Value of C**
Triangle	6.92820323
Quadrangle	4.0
Tetrahedron	124.70765802
Hexagon	41.56921938
Wedge	62.35382905
Pyramid	96

Aspect ratio is defined as the length of the longest side of an element divided by its shortest side. The value of skewness shows how close an element is to its ideal shape, where a value of 0 is perfect. Skewness can be calculated two different ways. The first method is called equilateral-volume-based skewness

$$Skewness = \left(\frac{Optimal\ Cell\ Size - Cell\ Size}{Optimal\ Cell\ Size}\right) \tag{12}$$

The optimal cell size for an individual element is an equilateral cell with the same circumradius as the cell size. The second skewness equation is the normalized-angular-skewness equation, (13) [27].

$$Skewness = maximum[\left(\frac{\theta_{max} - \theta_e}{180 - \theta_e}\right), \left(\frac{\theta_e - \theta_{min}}{\theta_e}\right)] \quad (13)$$

where θ_{max} is the maximum angle found in an element, θ_e angle of an equilateral element, and θ_{min} is the smallest angle of the element. Each of these angles is taken from individual faces of the elements [26].

Orthogonal quality is a value that ranges from zero to one, one as perfect. Figure 2.6, shows the vectors used to calculate element orthogonal quality [26].

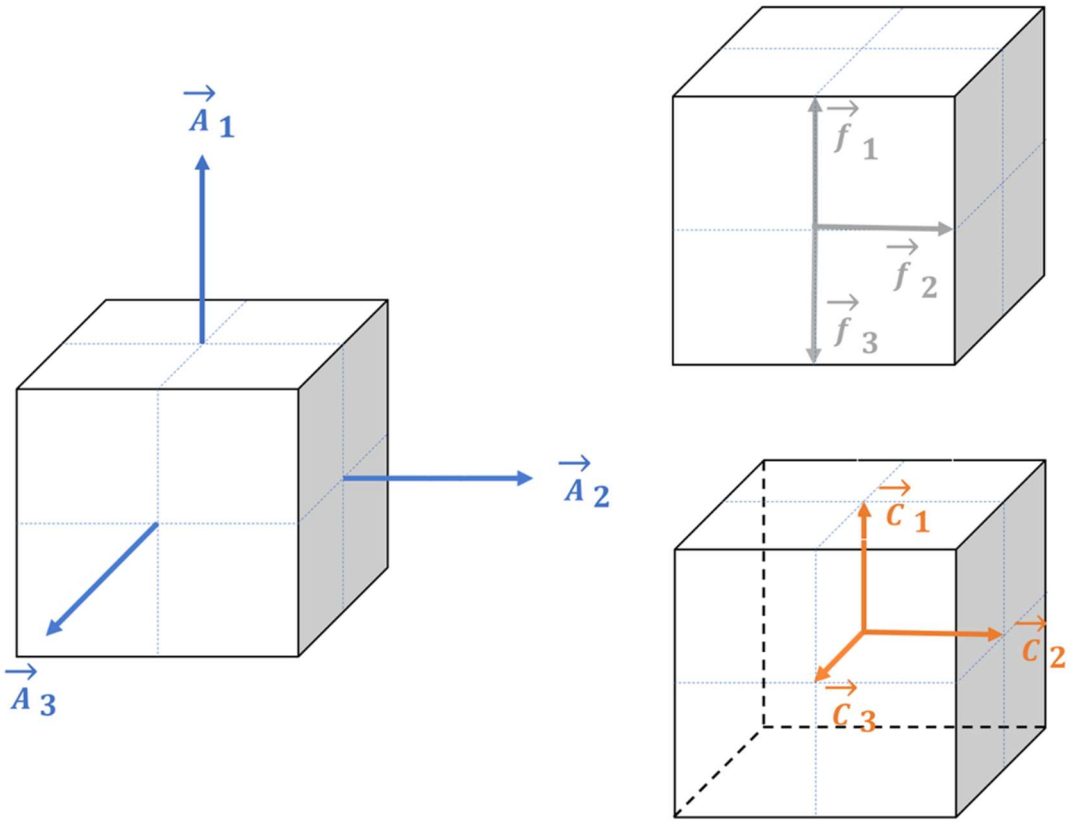

Figure 2.6 Orthogonal Quality Vectors of a Three-Dimensional Element

For an individual element, the minimum value of equations (14) and (15) is used as its orthogonal quality.

$$Orthogonal\ Quality = \frac{\overrightarrow{A_i} \cdot \vec{f_i}}{|A_i| \cdot |f_i|} \tag{14}$$

$$Orthogonal\ Quality = \frac{\overrightarrow{A_i} \cdot \vec{c_i}}{|A_i| \cdot |c_i|} \tag{15}$$

where the *c* vectors originate from the centroid of an element, the *f* vectors originate from the centroid of an individual face, and the *A* vectors are the face normal vectors.

Time discretization in finite element analysis involves choosing the proper time step interval for a transient analysis. The time step determines the duration of each load step and the total number of time steps determine the overall duration. Time steps should be such that the resulting frequency of the analysis is at least twice the frequency studied, this is known as the Nyquist sampling theorem [28].

In this study transient response analyses is used. Transient analysis of acoustical processes is carried out by solving:

$$[M]\{\ddot{u}\} + [C]\{\dot{u}\} + [K]\{u\} = \{f(t)\} \tag{16}$$

where $[M]$ is the mass matrix, $[C]$ is the damping matrix, $[K]$ is the stiffness matrix, $\{\ddot{u}\}$ is the nodal acceleration vector, $\{\dot{u}\}$ is the nodal velocity vector, $\{u\}$ is the nodal displacement vector, and $\{f(t)\}$ is the load vector [22]. Although this is the basic equation solved in transient analysis, the more equations that are involved simulation of a piezoelectric event are discussed in detail in a later chapter.

CHAPTER 3. ULTRASONIC TRANSDUCER CALIBRATION

The second focus of this dissertation is the creation of a novel method for calibrating preloaded transducers. The transducers in this study are calibrated for bone conduction testing in the ultrasonic human hearing range; however, the method presented in this dissertation has utility outside of this specific purpose, such as in micro crack detection.

3.1 Biomechanics of Hearing

The audible range of human hearing for air conducted frequencies is commonly classified between 20 and 20,000 Hz (20 kHz), and any frequency greater than this is considered ultrasonic. The audible frequency range is also known as the sonic hearing range [29]. Studies dated as far back as 1948 by Vladmir Gavreau and 1950 by R.J. Pumphrey, proposed that humans have some level of ultrasonic frequency detection through bone conduction [30, 31]. Bone conduction refers to a different method of frequency perception than the normal method of sound wave captured by the human ear. The sonic frequency hearing process is explained below.

As depicted in Figure 3.1, there are three sections of the human ear. The first section is called the external ear, and consists of the pinna and the auditory canal. The pinna, also known as the auricle, is the visible cartilage portion of the ear visible outside of the skull. It is meant to funnel sound waves into the ear auditory canal. The pinna is shaped in a way that is meant to favor sounds that correspond with the orientation of the head, which helps a person know the location of the sound course [32]. The auditory canal, also known as the external auditory meatus, transmits sound waves captured by the pinna to the middle ear.

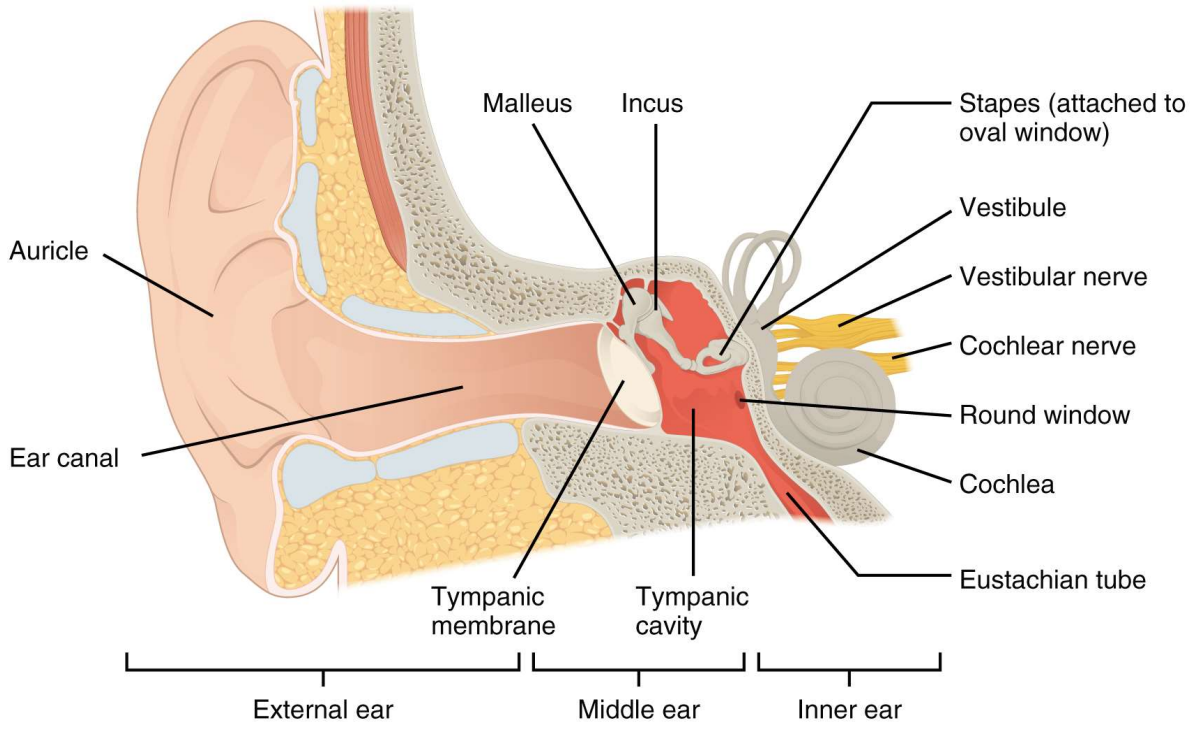

Figure 3.1 Human Ear Anatomy [33]

The second section is the middle ear. The middle ear is an impedance matching mechanism that creates a 30 to 33 dB gain between the air sound pressure waves captured by the external ear and the fluid contained in the inner ear. It consists of: the tympanic membrane, the malleus, the incus, the stapes, and the tympanic cavity. The tympanic membrane is stimulated by sound pressure waves that are captured and funneled by the external ear. Sound pressure waves cause the membrane to oscillate back and forth and this causes motion in the ossicular chain. Ossicles is the collective name of the three bones in the ossicular chain: the malleus, incus, and the stapes. These bones are the smallest in the body and are also respectively known as the hammer, anvil, and stirrup. They act as a three-bar mechanism responsible for converting the oscillations of the tympanic membrane into a stimulus that is sensed by the fluid of the inner ear. The tympanic cavity is the air-filled cavity containing the ossicles. This cavity is pressurized and is responsible for maintaining equalized pressure in the head.

There are three mechanisms in the middle ear that account for impedance matching and decibel gain. The first is the tip of the malleus that touches the tympanic membrane. This portion of the malleus is the manubrium. When the curved membrane vibrates from a sound pressure stimulus, the portion of the manubrium in contact with the membrane vibrates with less amplitude, but greater force than the surrounding membrane. This creates a ~6 dB gain. The surface area of the face of the stapes in direct contact with the inner ear is, on average, 18 times smaller than the effective surface area of the tympanic membrane. The reduction in area creates a ~25 dB gain. Finally, the lever action of the ossicular chain creates a ~2 dB gain.

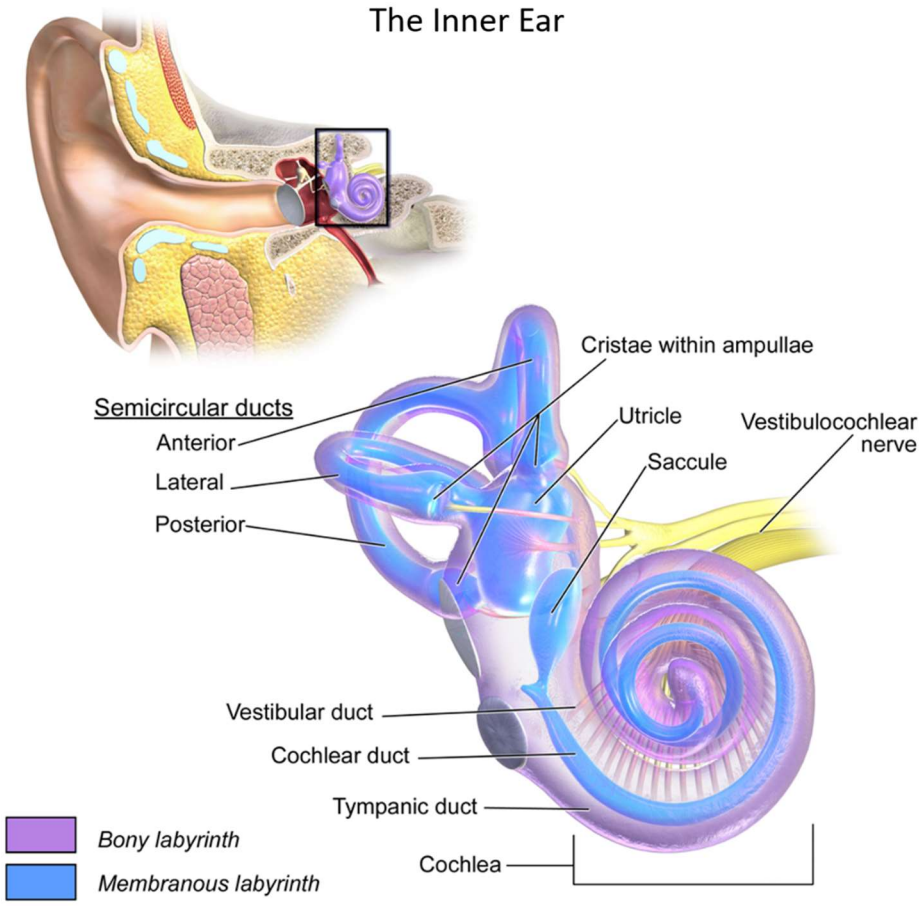

Figure 3.2 The Inner Ear Detail [34]

Figure 3.2 details the third section of the ear, the inner ear. The inner ear is composed of the bony labyrinth and the membranous labyrinth. These two labyrinths contain the vestibular

system and the cochlea, and are filled with perilymph and endolymph fluid [35]. The bony labyrinth is filled with perilymph fluid, while endolymph fluid fills the membranous labyrinth.

The vestibular system of the inner ear is not part of the hearing process, but rather, is used for balance. It contains the utricle, the saccule, and three semicircular canals. These canals are responsible for compensating for rotational movement. When the body rotates, this inner ear fluid rotates as well, and this creates a signal sent to the brain. Both the left and right side vestibular systems in the inner ear work simultaneously. The other two components of the vestibular system, the utricle and the saccule account for linear movements. Specifically, the utricle accounts for two-dimensional movement made on horizontal plane that intersects the skull, and the saccule accounts for two-dimensional movement made orthogonally to this plane [22].

The portion of the inner ear associated with sonic hearing is the cochlea. The cochlea is a snail shell shaped bony portion of the inner ear, and a cross section of the cochlea is depicted in Figure 3.3. This cross section clearly shows the complexity of the cochlear process. The membrane between the inner and middle ear that is in direct contact with the stapes is the oval window. Motion of the stapes in response to an acoustic stimulus leads to vibration of the oval window. The cochlea is comprised of three fluid filled chambers. One chamber (scala vestibuli) is bounded by the oval window and one end and the helicotrema at the other end. The second chamber (scala tympani) is bounded by the helicotrema at one end and the round window at the either end. Thus, the helicotrema allows the perilymph fluid in to fill both cavities. When the stapes vibrates, it leads to vibration of the oval window which produces vibration in the perilymph fluid filling the scala vestibuli and scala tympani.

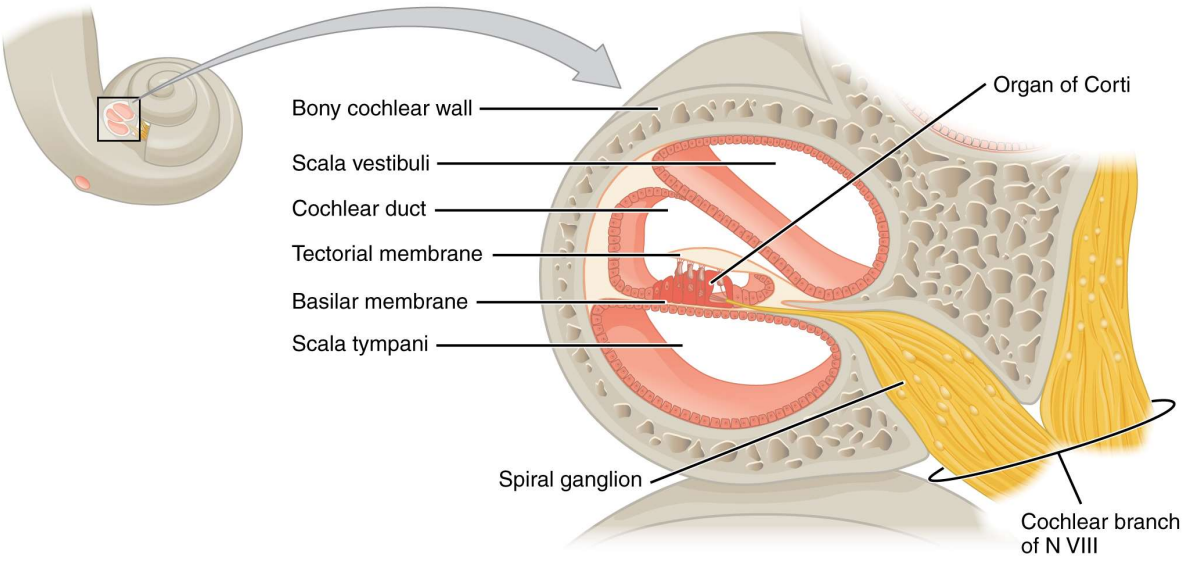

Figure 3.3 Cross Section of the Cochlea [33]

The vibration passes through the perilymph fluid in the scala vestibuli and the scala tympani, and create oscillations in both Reissner's membrane and the basilar membrane. These membranes separate the scala vestibuli and the scala tympani from the third chamber in the cochlea, the cochlear duct. As opposed to the other two chambers of the cochlea, the cochlear duct is filled with endolymph. The organ of corti, placed on top of the basilar membrane, vibrates in response to the oscillations created. The organ of corti is responsible for sending nerve impulses from the cochlea to the brain which are interpreted as sounds, via the cochlear nerve. These nerve impulses are created by bending of hair cells in organ of corti. The tips of these hair cells are embedded in the tectorial membrane and are bent from vibration of the basilar membrane. The basilar membrane itself is tonotopic meaning that the entire membrane does not vibrate simultaneously, this is due to varying stiffness. The membrane has higher stiffness close to the oval window and lower stiffness at its apex. The higher stiffness portion of the membrane perceives the upper end of sonic hearing, closer to 20 kHz, and the lower stiffness portion perceives the lower end of hearing, 20 Hz signals.

3.2 Bone Conduction Perception and Previous Studies

Typical hearing is completed by the process presented in the previous section; however, bone conduction provides a modified method of sound perception. A signal from a bone conducted vibration causes both the cochlea and the bone surrounding the inner ear to vibrate. By vibrating the cochlea directly, the external and middle ear are not utilized since there is no sound pressure wave that needs to be captured and converted into a mechanical stimulation. This occurs naturally, especially for body-generated sounds such as speech, and for loud sounds in the environment. Bone conduction for body-generated sounds has relatively low impedance, and is efficiently transmitted to the fluid-filled cochlea. External acoustics stimulation is transmitted more efficiently through the ear canal and middle ear than through vibrations of the skull or other bones connected to the skull.

Conventional understanding dictates that the limit of sonic hearing is around 20 kHz; however, studies have shown that, through bone conduction, ultrasonic hearing is possible above 20 kHz. Although this is not entirely understood, several theories have arisen to explain this phenomenon. In 1963, Daeff and Knox theorized that the bone conduction when interacting with blood, tissue, and musculature resulted in ultrasonic resonance in the (peripheral, central, or both) auditory system. Further, in a 2003 study, Lenhardt hypothesized that ultrasound conducted through the bone could resonate in the skull generating signals that can be interpreted through the cochlea [36]. Another theory by Nishimura concluded that the hair cells of the basilar membrane vibrated directly from a bone conducted signal causing ultrasonic perception [37]. Although there is not a definitive answer, most theories conclude that if ultrasonic hearing is somehow captured by the normal auditory system, it is because of direct resonance of the inner ear. These theories are based on the observation that, when a human senses an ultrasonic signal, it is perceived as a

louder sound than the highest sonic frequency a person can hear [38]. As the frequency increases, the subject senses the same sound frequency, only with changes in loudness perception [29]. For instance, if a subject's sonic hearing threshold is 20 kHz, when they perceive an ultrasonic signal it will sound the same as the 20 kHz signal, but with a higher amplitude.

An alternate explanation for ultrasonic hearing states that the vestibular system, rather than the cochlea, interprets these signals. In 1991, Lenhardt conducted a study that included both elderly hearing impaired and profoundly deaf subjects, between the ages of 50 and 82. The study compared the ultrasonic frequency perception of this group and a group between the ages of 20 and 29 years old with no hearing loss. The results showed that the ultrasonic hearing thresholds of these groups were similar, regardless of hearing impairment in the sonic hearing range. The experiment further tested the ability of these groups to understand words when using ultrasonic frequencies. The results showed that test subjects could successfully identify the word transmitted at ultrasonic frequencies between 45 and 70 percent of the time. This study lead Lenhardt to hypothesize that ultrasonic frequency recognition could also be the result of secondary signal generation from the vestibular system to the brain.

3.3 Previous Audiological Bone Conduction Transducer Calibrations

A necessary step before testing any type of bone vibrator on human test subjects is threshold calibration. This process is used to measure hearing threshold levels against reference threshold levels in order to keep testing procedures consistent; however, there are no threshold standards for ultrasonic bone conduction [36]. Thresholds are defined as the softest sound that are heard by a subject. Thresholds for detecting bone-conducted stimuli are usually measured for a series of different tonal frequencies and are expressed in terms of decibels either in units of sound pressure (i.e, micro Pascals) generated in a water filled cavity containing the bone conduction

transducer or force measured via accelerometer. To date, there are no standards for calibrating ultrasonic stimulation.

In an early bone conduction test, J. F. Corso calibrated transducers measuring their sound pressure levels [7]. The transducer tips were placed in a three-cubic foot water tank, and a frequency response curve was created for the range of 5 kHz to 100 kHz. The frequency response was captured in terms of sound pressure level. The water tank used in his study mimics the impedance characteristics of bone and tissue.

A similar calibration procedure was performed by Koizumi [39]. In Koizumi's study, a hydrophone was placed in a tank of degassed water. This tank recorded acoustic outputs and was placed 100 mm away from the end of an ultrasonic transducer. The transducer created 500 millisecond long duration 30 kHz signals. In this study, the water tank was used to ensure that the ultrasonic transducer was not creating any audible air conducted sound. An audible sound would affect threshold measurement for bone conducted ultrasound since it could create confusion, making it more difficult for a test subject to correctly identify an ultrasonic bone vibration.

Lenhardt carried out a bone conduction calibration in 2002 that utilized an accelerometer. In this study, a Brüel & Kjær 4374 accelerometer was placed between a human head and a Radioear B-71 bone vibrator. The bone vibrator and accelerometer were held in place on the head with a prestressed metal head band. The calibrations used in this study were performed only at 6 kHz, and were used as reference levels for a second bone vibrator device used for tinnitus therapy. The second bone vibrator was calibrated in the sonic range, from 6 kHz to 20 kHz using the same equipment and methods. [36].

In each of these calibration procedures, there is an oversight that does not address the operation conditions of the transducer. In two of these studies, the transducers were calibrated by

sounds pressure level; however, what is of interest is the vibration created by the transducers when placed in contact with a person's skull. If the transducers were utilized for transmission of air conducted ultrasonic signals, these calibrations would be sufficient, but sound pressure levels should not be the focus of bone conducted signal calibration. The calibration methodology employed by Lenhardt came closer to classifying the bone conducted signal; however, it was completed only in the sonic range of hearing, and the accelerometer utilized was fixed at both ends, which may have affected the calibration results. For these reasons, the methodology presented in Chapter 4 was created.

CHAPTER 4. ULTRASONIC TRANSDUCER CALIBRATION

This chapter describes the procedures developed for the calibration of an ultrasonic transducer. Previous studies, specified in CHAPTER 3, either have not focused on ultrasonic calibration, or have not accounted for the operation conditions of the accelerometer. Although this chapter describes calibration of ultrasonic bone conductors, these procedures can be adapted for calibration of any transducer that will have a static load applied to its actuating face.

4.1 Calibration Procedure

Our area of interest for ultrasonic characterization is the interval from 20 kHz to 80 kHz. After a comprehensive search and characterization of several transducers, transducer model SMUTF40FTR15B made by Steiner and Martins Inc in Doral, Florida was selected to be optimum for our ultrasonic bone conduction studies and calibrated in detail. This transducer has a reported central operating frequency of 40 kHz.

The calibration of this transducer was comprised of two separate steps. In the first step, the free response of the transducer was recorded; in the second step, the response of the transducer under a static applied load was recorded. The free response of the transducer is the ultrasonic frequency response characterization with an accelerometer, but with no static load applied. To calibrate the free response of the transducer, the testing apparatus depicted in Figure 4.1 Schematic Diagram of Calibration Set up for Unloaded Transduceris utilized. The results of this unloaded transducer response were recorded to compare the variation created in the transducer's operation when a static load is applied to its operating face.

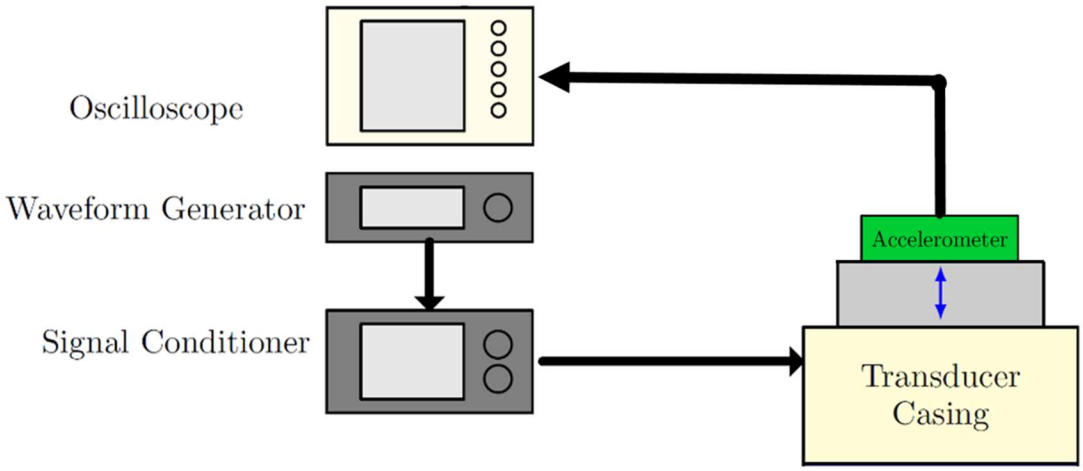

Figure 4.1 Schematic Diagram of Calibration Set up for Unloaded Transducer

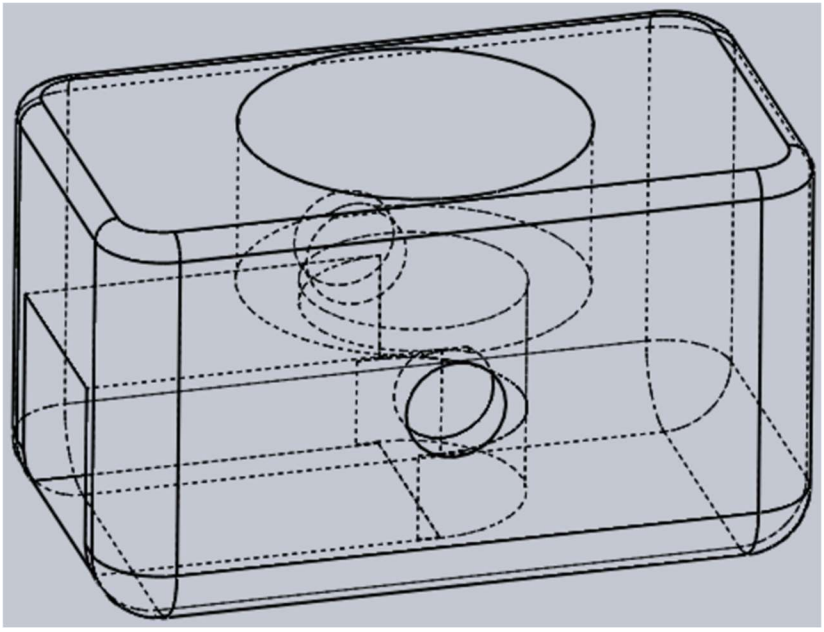

Figure 4.2 CAD Model of Custom Designed ABS Plastic Transducer Casing

In Figure 4.1 the waveform generator, Agilent model 33210A, was connected via BNC to SMA cable to the transducer. The transducer was placed inside of a 3-D printed acrylonitrile butadiene styrene (ABS) plastic, seen in Figure 4.2. This casing was modeled after the commercially available RadioEar B71 bone vibrator casing. A PCB PIEZOTRONICS miniature

teardrop accelerometer was placed on the exposed actuating face of the transducer, and was coupled with a very thin layer of Sonotech SOUNDSAFE ultrasonic coupling gel. The miniature accelerometer was then connected to a PCB model 480C02 ICP sensor signal conditioner. Finally, the output of the signal conditioner was connected to an Agilent Technologies model DSP-X 3042A digital storage oscilloscope. The calibration was carried out applying a 500 mVpp [millivolt peak to peak] signal from the waveform generator to the transducer for frequencies ranging from 20 kHz to 103 kHz. The frequency was increased in steps of 1 kHz, adjusting the signal amplitude after each response was recorded. The calibration exceeded the desired range of 80 kHz to acquire a more complete frequency response curve of the transducer. Figure 4.3 Unloaded Frequency Response Curves of Transduceris the calibration curve of the free-response of the transducer. The figure's *x*-axis is the frequencies applied to the transducer by the waveform generator, and its *y*-axis represents the relative decibel voltage drop at each individual frequency.

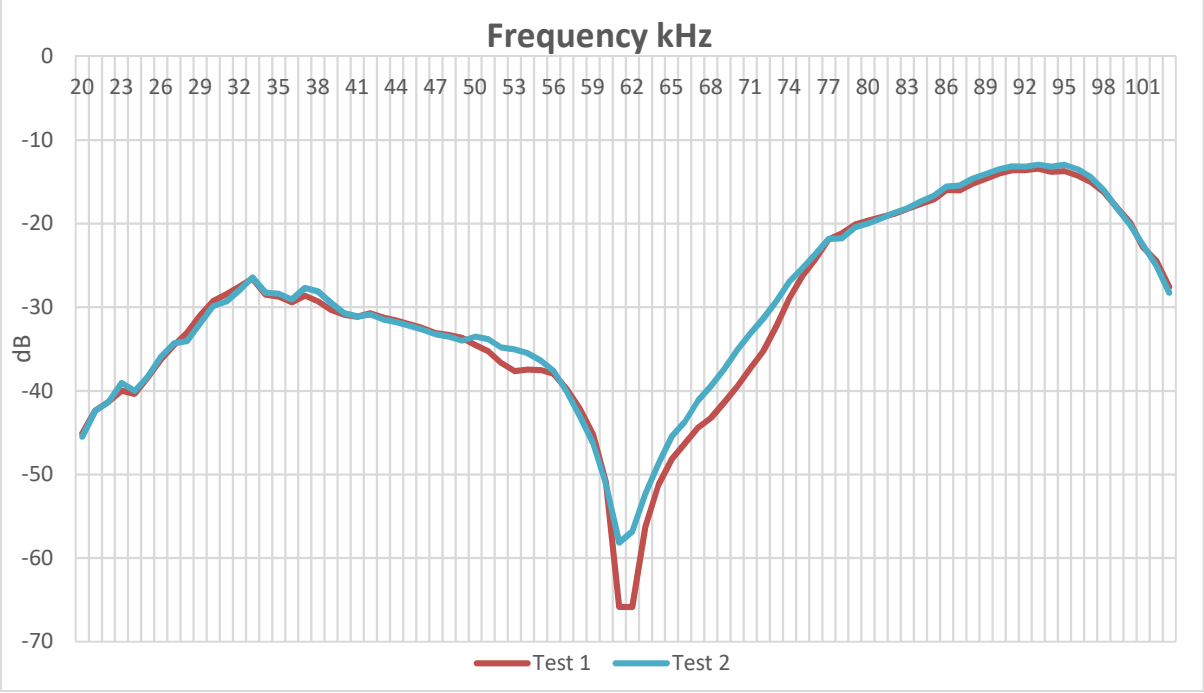

Figure 4.3 Unloaded Frequency Response Curves of Transducer

The second half of the calibration procedure was performed to obtain the response curve of the transducer while placed under a static load. A common method of bone conduction calibration is the use of an artificial mastoid, such as the Bruel and Kjaer model 4930. The artificial mastoid is meant to simulate the impedance characteristics of the human head, and translates mechanical vibrations from bone oscillators into an electrical charge by thin piezo electric disks. This charge is converted into a voltage and then into a force that is in dB using equation (17).

$$F_{dB} = 20\log_{10}\left(\frac{F_{measured}}{F_o}\right) \tag{17}$$

A key characteristic in the calibration method of the model 4930 artificial mastoids is applying a constant 5.4 N force to the bone oscillator. This force is applied via a weight. The limitation of existing methodology for calibration of bone vibrators is that artificial mastoids are only meant to operate in the sonic hearing range. The human hearing range reaches approximately 20 kHz, because of this there is typically no need to calibrate bone oscillators into the ultrasonic range. To characterize the effects of ultrasonic signal transmission, a new method of calibration had to be developed. The calibration method depicted in Figure 4.4 Schematic Diagram Calibration Set up for Loaded Transducerwas created to address this limitation: This method expands upon the basic calibration of the unloaded transducer through the addition of a regulated static force. This force is monitored by a Wheatstone bridge type force sensor. This force sensor utilizes an array of resistors, which have a constant direct current voltage applied to them. When there is no load applied to the sensor, the resistors divide the voltage evenly; however, when the resistors are bent in response to a force applied to the sensor, the resistors compress, or are placed in tension, which effects the voltage division. This variation in voltage division is then used to calculate the amount of load placed on the sensor.

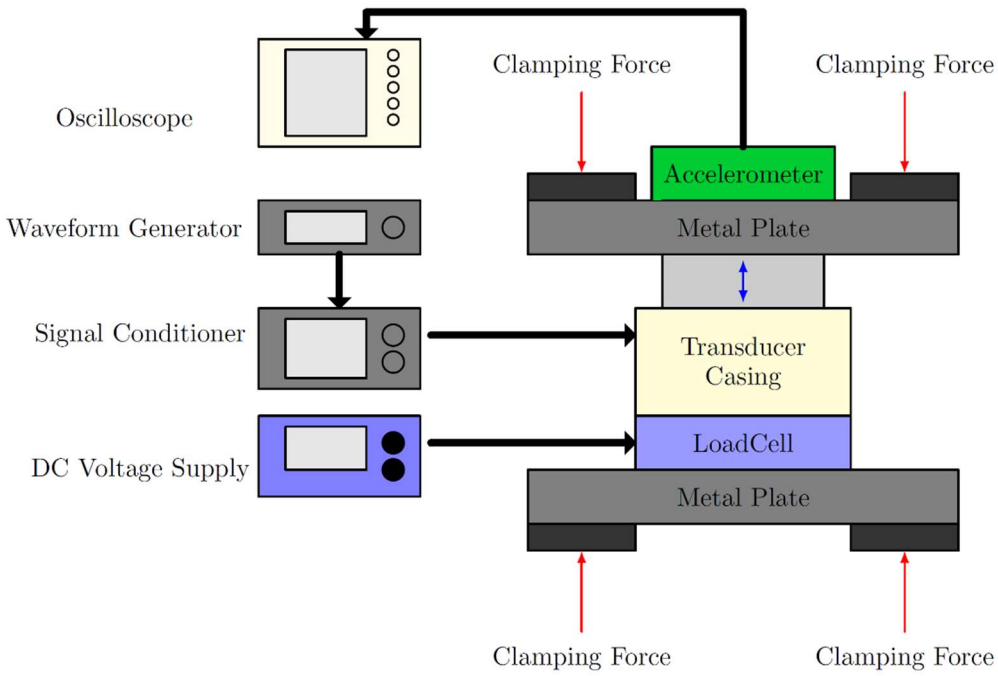

Figure 4.4 Schematic Diagram Calibration Set up for Loaded Transducer

This calibration method requires a stabilization rig, a force sensor, a constant voltage supply, a digital multimeter, and two thin steel sheet metal plate. In this methodology, a sheet metal plate was used in the place of a bulkier weight in order to minimize the distance between the transducer and the accelerometer meant to characterize its frequency response. When a bulkier weight was used to apply the static load, the accelerometer was unable to capture any response information when the transducer was actuated. The amount of clamping force applied from the sheet metal plate to the transducer was regulated by tightening and loosening the four nuts located on the corners of the stabilization rig. The force regulating nuts are seen more clearly in Figure 4.5 Finalized Calibration .

A major hurdle that needed to be overcome was the development of a method of consistently applying a static load level to the transducer. The stabilization rig shown in Figure 4.5 Finalized Calibration successfully addressed this issue.

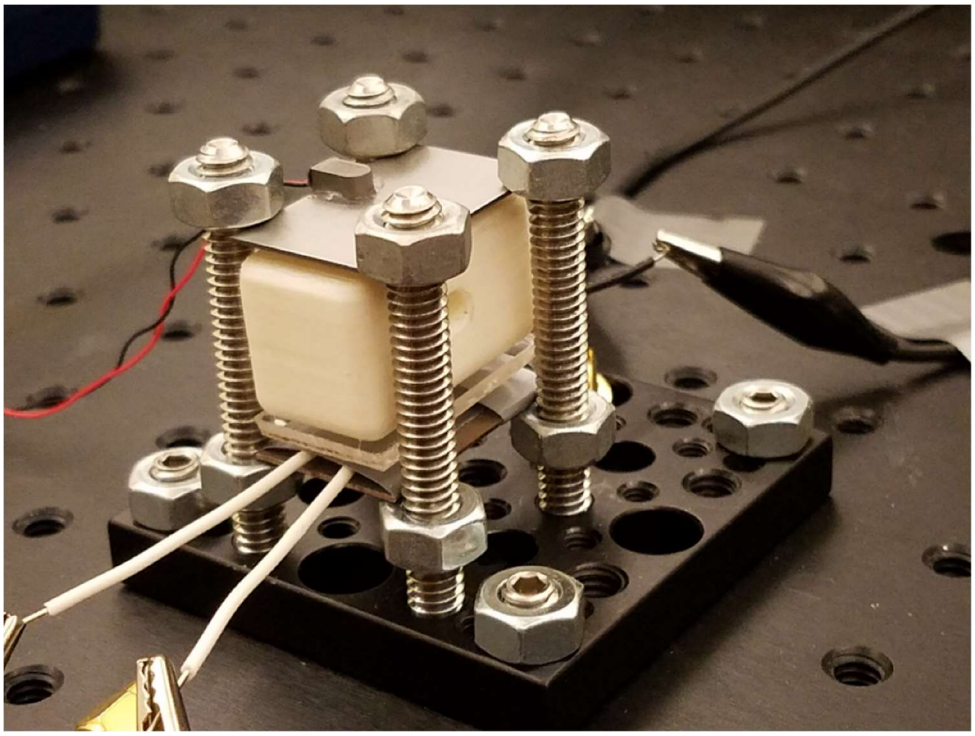

Figure 4.5 Finalized Calibration Apparatus

The rig minimizes any unnecessary vibrations during calibration, as well as providing a means of applying a constant force to the transducer face. At the bottom of the rig, a Honeywell model FSS1500NST force sensor was placed on top of a flat piece of sheet metal. The sheet metal serves as a base for the rig, and ensures that the force sensor stays level. The Honeywell force sensor is a push button, Wheatstone bridge type, and has a nominal sensitivity of 0.12 mV/gram. The base of the transducer case was a rough surface; this is a result of the 3-D printing process. The force sensor is very sensitive to surface flatness, therefore a small piece of plexiglass plastic was affixed to the bottom of the transducer case. The force sensor exhibited a small decay with time in the force readings applied to it, the procedure to account for this decay is detailed later in this chapter.

Figure 4.6 Frequency Response Curves of Transducerand Figure 4.7 Error Bars of Statically Loaded Transducercontain the results of five separate tests in the response of the transducer from 20 kHz to 80 kHz.

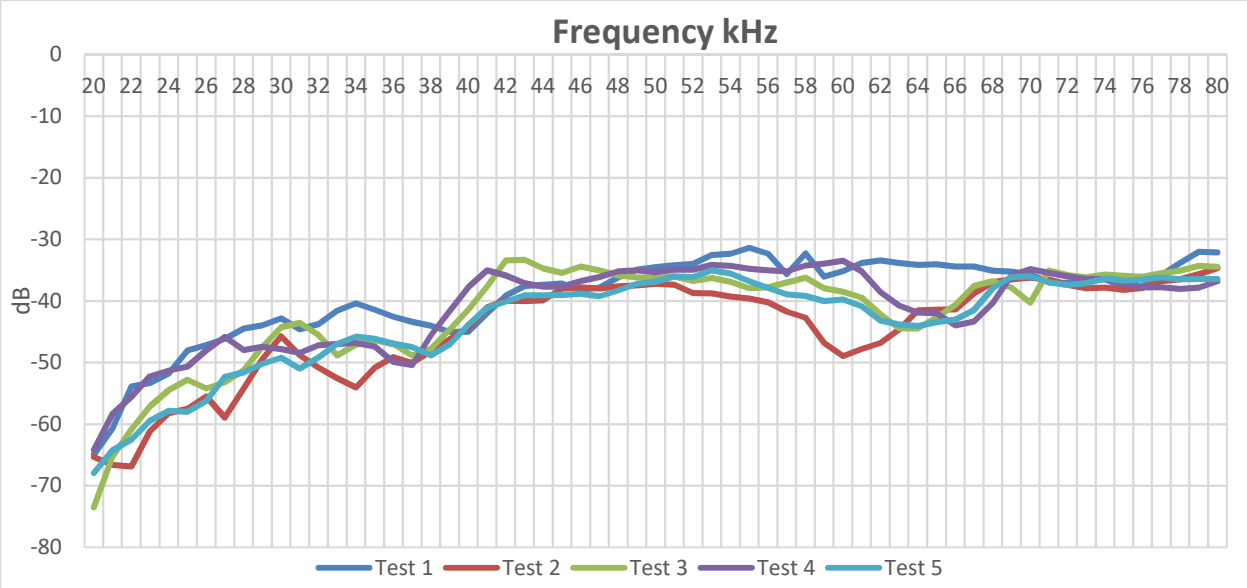

Figure 4.6 Frequency Response Curves of Transducer Under Static Load

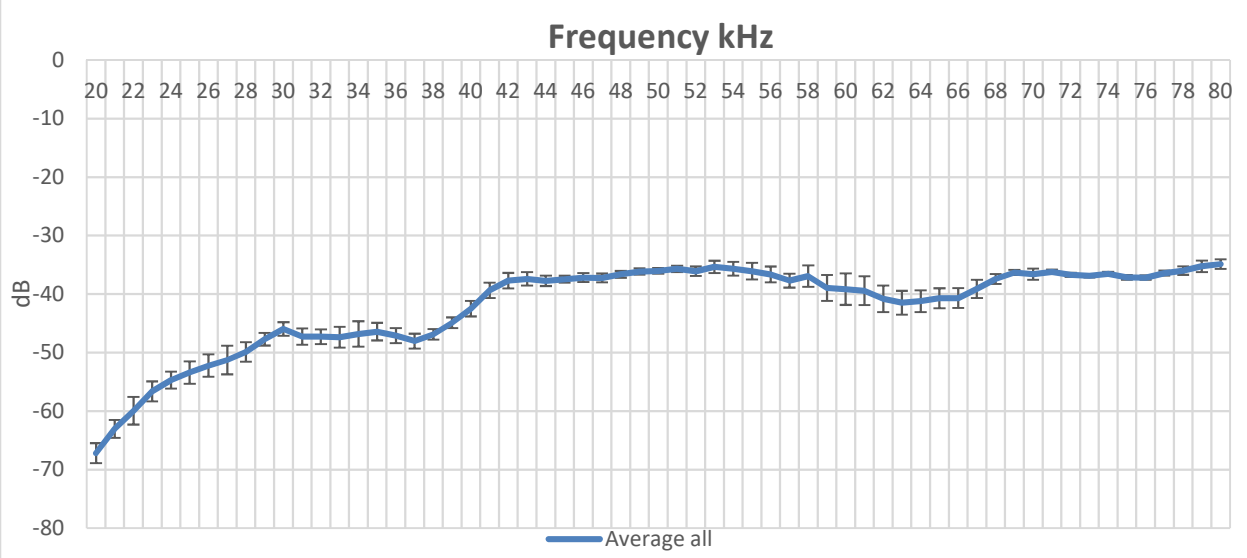

Figure 4.7 Error Bars of Statically Loaded Transducer

The calibration of the loaded transducer shows significant variation from the frequency response of the unloaded transducer, and this response varies as the static load applied to its

actuating face is altered. As the load level increases, the total response curve broadens within the -40 to -50 decibel range; conversely, as the load decreases, the frequency response approaches the shape of the unloaded calibration curve. The loaded response curves presented in Figure 4.6 and Figure 4.7 validate the need for the creation of this novel method of calibration for ultrasonic bone conducting transducers. As the transducers are, in the future, used for testing on human patients, it is imperative that the signal they create are definitively known in order to properly measure the levels and types of bone conducted signals a subject perceived.

4.2 Static Force Calibration

For the calibration study conducted in section 4.1, a thorough investigation was completed to ensure stability with the applied static load. The level of applied load required to correctly mimic the loads that the bone conducting transducer would experience in operation is significant. Initial testing showed a rapid decrease in the load amount that was sensed by the Honeywell force sensor after the peak load level was applied. The exact cause of this decay was not determined; however, the decay rate was found as a function of time through experimentation. A possible cause of this decay however can be attributed to the RC time constant of the circuit inside of the force transducer itself. There is a time constant associated with both charge and discharge of a voltage applied, and this is a potential cause of the decay rate of force measured [40]. This rate is shown in Figure 4.8 and Figure 4.9. Figure 4.8 depicts an entire decay rate measurement of the force sensor, whereas Figure 4.9 shows a linearization of the decay rate as time progresses. This linearization allowed for easy prediction of the total amount of decay in the level of force read, as well as minimization of the force decay experienced as calibration of the transducer took place. Minimizing the load variation was key to assuring constant and repeatable calibration attempts.

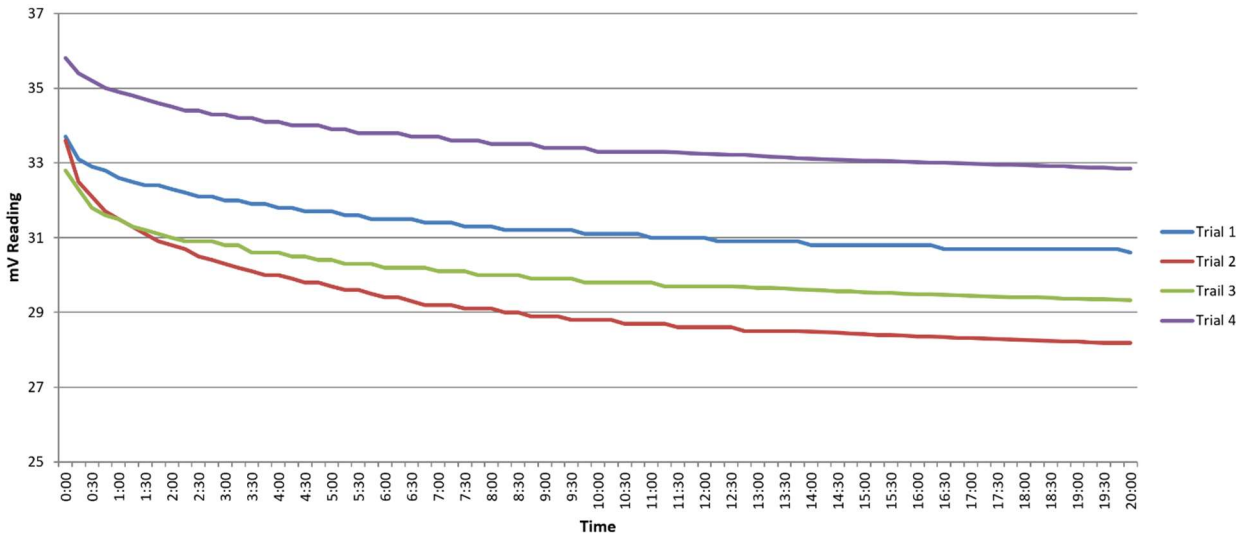

Figure 4.8 Stabilization Rig Calibration Force Decay Rate

Figure 4.8 depicts the decay rate of the force readings from the Honeywell force sensor. The force sensor in this application was supplied a constant 2 V_{dc}. After adjusting the tightness of the four force regulating nuts on to achieve a peak load level, voltage readings were taken from the force sensor every fifteen seconds for twenty minutes. Four separate trials showed that the force decay rate slowed considerably after the ten-minute mark. Figure 4.9 shows the force readings only between ten and twenty minutes for these same trial results.

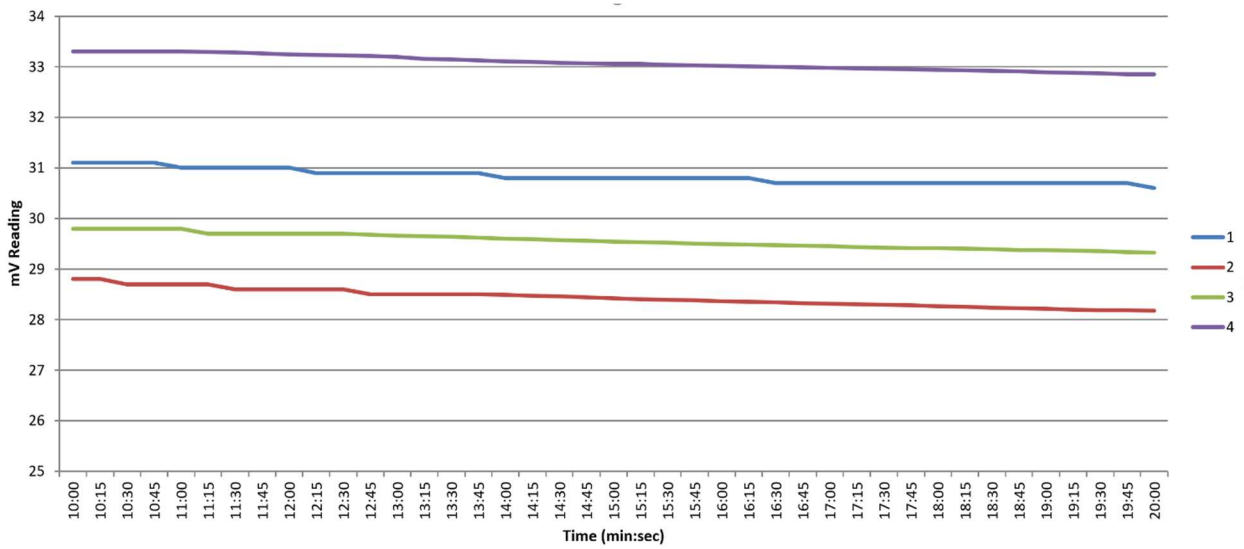

Figure 4.9 Calibration Force Decay Rate from 10 to 20 Minutes

The preceding figures clearly indicate that, with longer settling times after application of an initial force load to the transducer, the decay rate slows down and becomes linear. A decay of 0.5 millivolts over ten minutes, when the sensor is supplied with a constant 2 V_{DC}, is equivalent to a 10.4 gram decrease in mass applied to the transducer. With measurements starting at 520 total grams applied to the transducer this drop is a 2.04% decrease. The force level that is applied to the transducer during ultrasonic bone vibrations by the prestressed metal head band, described in Chapter 3.3 is equal to the 5.1 Newtons, which corresponds to the 520 grams of preload. Given this information, every calibration procedure completed in chapter 4.1 was made after two conditions were met. The first condition was that the load level had reached an equivalent of 520 grams, and the settling time for the load to reach this level was a minimum of 20 minutes.

CHAPTER 5. SURFACE ACOUSTIC WAVE MODELING

5.1 Introduction

Surface acoustic wave (SAW) devices are subset of micro electromechanical systems (MEMS) that are used for signal processing [41, 42], chemical analysis [43, 44] and biomedical applications [19, 45-51] via exciting surface waves on piezoelectric substrates. The substrate is stimulated by pairs of conductive thin film interdigital transducers (IDTs) with width and pitch that are designed to excite desired frequencies. The waves that propagate on the surface of the substrates are confined within a layer under the surface which has a thickness close to one wavelength [52]. The superficial character of these waves provides sensitivity to alterations in physical quantities such as temperature, strain, and mass changes on the surface of the substrate [14,15].

Recently, attention has been focused on the modelling of SAW devices via mathematical and numerical modelling techniques [14–23]. Numerical techniques include Finite Element Method (FEM) [14–19], Finite Difference (FD) [53] and the Boundary Element Method (BEM) [21] or a combination of FEM and BEM [22,23]. Among these techniques, FEM is widely used to model SAW devices in both 2 and 3 dimensions. Often the SAW devices are limited to models only consisting of piezoelectric substrate and IDTs. Generally, the effects resulting from pressure, mass or viscosity are overseen in models; however, Atashbar et al. [53] studied a 3-Dimensional finite element model of XY-cut $LiNbO_3$ SAW hydrogen sensor with a palladium (Pd) thin film developed on the substrate. The insertion loss (IL) and the impulse response of the device were

simulated in this work. The effect of exposure was achieved via changing the density and thickness of the Pd thin film.

Xu [53] presented a direct finite element model for predicting the characteristic response of the YZ-cut $LiNbO_3$ SAW filter. In the study, equations of motion that define the mechanical behavior are coupled with Maxwell's equations for electromagnetic behavior, to model the propagation of acoustic waves in piezoelectric media. The Rayleigh damping coefficients were implemented to reduce the interference of the waves reflected from the boundaries. Fourier transform of the impulse response was used to acquire the frequency response of the filter. Ippolito et al. [53] reported a 3-Dimensional simulation of a XY-cut $LiNbO_3$ layered SAW device which was studied in ANSYS® software package. The SAW device consisted of two IDT pairs in each port that were patterned on the surface of the $LiNbO_3$ substrate, i.e. the transmitting and receiving ports, and a 3 mm thick ZnO guiding layer. One of the conclusions of this research was that finite element modelling packages are effective ways for a deeper understanding of SAW phenomena in piezoelectric media. In their finite element analysis study, Abdollahi et al. [19] evaluated the mass sensitivity of SAW sensors with various piezoelectric materials i.e. lithium niobate, quartz, lithium tantalate and langasite. Similar to earlier research studies, they investigated the impulse response and the insertion loss of the SAW filters. In a recent research paper, Gowini and Moussa reported a Finite Element Analysis of a SAW Hydrogen Sensor which was modeled using ANSYS® [15]. The SAW sensor they modeled consisted of a YZ-cut $LiNbO_3$ substrate and a thin palladium film. They presented the IL via obtaining the frequency response from the time domain response by Fourier transform.

In this chapter, an investigation of the effect of PDMS channel side wall thicknesses for acoustic microfluidic devices via simulating the insertion loss by 3-Dimensional Finite Element

Modelling is carried out. The simulation study was carried out in two main steps; first, a calibration step of bare 128_YX-cut $LiNbO_3$ for obtaining the boundary conditions and second, with the PDMS channels constructed on the substrate. The PDMS channel side wall thickness was varied between 2 mm and 8 mm and the results were compared with experimental results of a prior study.

5.2 Design Variables

To mathematically model the wave propagation in piezoelectric solids, mechanical and electrical effects have to be taken into account which are governed by equations of motion and Maxwell's Equations, respectively [10, 54-57].

The Heckmann Diagram shows the interrelationships between electrical, mechanical, and thermal properties of materials. Figure 5.1 is the part of the Heckmann Diagram composed of the mechanical and electrical properties.

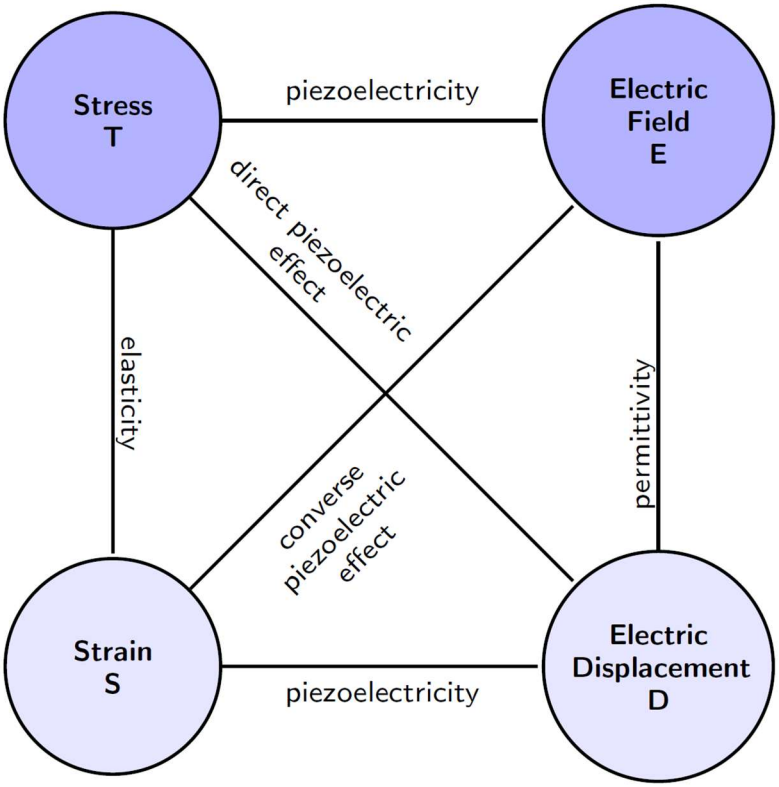

Figure 5.1 Partial Heckmann Diagram

From this diagram, the constitutive equations for the electromechanical effects in piezoelectric transducers can be derived in matrix form as

$$D_m = e_{mkl}S_{kl} + e_{mj}E_j \tag{18}$$

for the direct piezoelectric effect and

$$T_{ij} = e_{mkl}S_{kl} + e_{mj}E_j \tag{19}$$

for the converse piezoelectric effect. Here D is the dielectric displacement (or the polarization), e is the piezoelectric stress coefficient, E is the electric field, ε is the material's dielectric constant, T is the stress and S is the strain. Using equation (19), one can then write Newton's Second Law of motion as

$$\rho\ddot{u}_i = \frac{\partial T_{ij}}{\partial z_j} = c_{ijkl}\frac{\partial S_{kl}}{\partial z_j} - e_{mij}\frac{\partial E_m}{\partial z_j} \tag{20}$$

here, z_j is the coordinate component of the particle of interest. With the assumption that there are no electrical charges present on the surfaces of the piezoelectric substrate and using equation (18), Maxwell's Equation can be defined by

$$\frac{\partial D_m}{\partial z_j} = 0 = e_{jkl}\frac{\partial S_{kl}}{\partial z_j} - e_{mj}\frac{\partial E_m}{\partial z_j} \tag{21}$$

In terms of displacement (u_k) and electric potential (f), strain and electric field are given by

$$s_{kl} = \frac{\partial u_k}{\partial z_l} \tag{22}$$

and

$$E_m = -\frac{\partial \phi}{\partial z_m} \tag{23}$$

respectively. Substituting Equations (22) and (23) into Equations (20) and (21), we can rewrite the equations as

$$\rho\ddot{u}_i = c_{ijkl}\frac{\partial^2 u_k}{\partial z_j \partial z_l} + e_{mij}\frac{\partial^2 \phi}{\partial z_j \partial z_m} \tag{24}$$

$$\frac{\partial D_m}{\partial z_j} = 0 = e_{jkl}\frac{\partial^2 u_k}{\partial z_j \partial z_l} + \varepsilon_{mj}\frac{\partial^2 \phi}{\partial z_j \partial z_m} \tag{25}$$

Considering plane waves in piezoelectric media, the solutions of these equations are

$$u_k = A_k \exp i(\omega t - k_i z_i) \tag{26}$$

and

$$\phi = \Phi \exp i(\omega t - k_i z_i) \tag{27}$$

where w is the radial frequency, t is time and k_i is the wave number. The solutions for equation (26) relate to the acoustic waves while the solutions for equation (27) are related to the electromagnetic waves [24,25].

The substrate material used in this study is 128°YX-cut $LiNbO_3$. Single crystal $LiNbO_3$ has trigonal symmetry and belongs to the point group 3m. According to Neumann's principle, any physical property of a crystal must include the symmetry elements of the crystal itself. Thus, the elastic constants (c_{ij}), the piezoelectric stress constants (e_{ij}) and the dielectric constants (ε_{ij}) in matrix form are given in Figure 5.2. This represents the generalized form of the constants used for lithium niobate. When the values in this figure are replaced with the numerical values presented in Table 5.1 Property Constants of $LiNbO_3$they must then be transformed to properly represent the values for 128°YX-cut $LiNbO_3$. This is completed through the use of Eulerian angles, which allow for the creation of the three specific direction cosine matrices needed to transform the properties to their proper crystallographic orientation. The Eulerian angles as well as transformations are detailed in Figure 5.3 and equations (28) through (30).

$$c_{ij} = \begin{bmatrix} c_{11} & c_{12} & c_{13} & c_{14} & 0 & 0 \\ c_{12} & c_{11} & c_{13} & -c_{14} & 0 & 0 \\ c_{13} & c_{13} & c_{33} & 0 & 0 & 0 \\ c_{14} & -c_{14} & 0 & c_{44} & 0 & 0 \\ 0 & 0 & 0 & 0 & c_{44} & c_{14} \\ 0 & 0 & 0 & 0 & c_{14} & \frac{1}{2}(c_{11} - c_{12}) \end{bmatrix} N/m^2$$

$$e_{ij} = \begin{bmatrix} 0 & 0 & 0 & 0 & e_{15} & e_{22} \\ -e_{22} & e_{22} & 0 & e_{15} & 0 & 0 \\ e_{31} & e_{31} & e_{33} & 0 & 0 & 0 \end{bmatrix} C/m^2$$

$$\varepsilon_{ij} = \begin{bmatrix} \varepsilon_{11} & 0 & 0 \\ 0 & \varepsilon_{11} & 0 \\ 0 & 0 & \varepsilon_{33} \end{bmatrix}$$

Figure 5.2 Generalized Piezoelectric Matrices

Table 5.1 Property Constants of $LiNbO_3$

Constant	Value
c_{11}	$2.03\times10^{11}\frac{N}{m^2}$
c_{12}	$0.573\times10^{11}\frac{N}{m^2}$
c_{13}	$0.752\times10^{11}\frac{N}{m^2}$
c_{14}	$0.085\times10^{11}\frac{N}{m^2}$

Table 5.1 Continued

c_{33}	$2.424\times10^{11}\frac{N}{m^2}$
c_{44}	$0.595\times10^{11}\frac{N}{m^2}$
e_{15}	$3.7\frac{C}{m^2}$
e_{22}	$2.5\frac{C}{m^2}$
e_{31}	$0.23\frac{C}{m^2}$
e_{33}	$1.33\frac{C}{m^2}$
ε_{11}	44
ε_{33}	29

As the substrate is 128° YX-cut $LiNbO_3$, the constant matrices must be transformed to the orientation of the crystal cut. The Eulerian angles (θ, ϕ, ψ) and the rotations required for the transformations are given in Figure 5.3. For the 128° YX-cut $LiNbO_3$ the Eulerian angles are (0°, 38°,0°). These rotations are completed in three stages, where a primary set of orthogonal axes are transformed into a new set of orthogonal axes by creation of one new axis per a stage for each Eulerian angle rotation required. In Figure 5.3 this is demonstrated as the original set of axes *X Y* and *Z* are transformed into a final set of axes through rotations of angels theta, phi, and psi into X''', Y''', and Z'''.

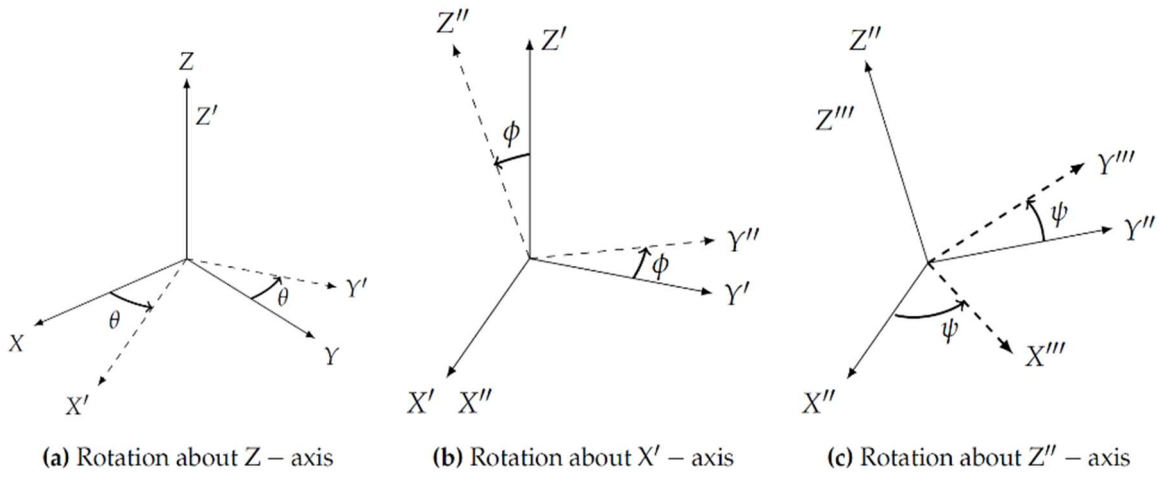

(a) Rotation about Z – axis **(b)** Rotation about X′ – axis **(c)** Rotation about Z″ – axis

Figure 5.3 Eulerian Angle Rotations

For obtaining the transformed matrices, one must employ direction cosines (a_{ij}; i, j = 1,2,3) [53] and use the relations given in equations (28) through (30) as

$$(c') = (a)(c)(\alpha) \tag{28}$$

$$(e') = (a)(e)(\alpha) \tag{29}$$

$$(\varepsilon') = (a)(\varepsilon)(\alpha) \tag{30}$$

where the transformed property matrices are given with primed letters and (a) and (α) are the direction cosine matrix and the transformation matrix, respectively. The transformation matrix is directly related to the specific point group of a given crystal geometry. In the case of lithium niobate, the point group is 3m, or the trigonal crystalline point group. This point group further denoted the amount of transformations necessary for determination of a material property in any given direction. Therefore, transformed matrices for elastic, piezoelectric and dielectric constants are obtained and shown in their finalized format in Figure 5.4. Here the matrix "*c*" is in units of force per unit area, and matrix "*e*" is shown in coulombs per unit area, or the amount of electric charge per unit area in a substrate caused by the piezoelectric effect.

$$c_{ij} = \begin{bmatrix} 2.03 & 0.7233 & 0.6017 & 0.1074 & 0 & 0 \\ 0.7233 & 1.9428 & 0.9061 & 0.0894 & 0 & 0 \\ 0.6017 & 0.9061 & 2.203 & 0.0812 & 0 & 0 \\ 0.1074 & 0.0894 & 0.0812 & 0.7491 & 0 & 0 \\ 0 & 0 & 0 & 0 & 0.7803 & -0.3222 \\ 0 & 0 & 0 & 0 & -0.3222 & 1.1162 \end{bmatrix} \times 10^{11}\ N/m^2$$

$$e_{ij} = \begin{bmatrix} 0 & -1.8284 & 1.7204 \\ 0 & 4.4506 & -2.6562 \\ 0 & -1.5202 & 2.3464 \\ 0 & 0.0782 & 0.6162 \\ 4.4548 & 0 & 0 \\ 0.3079 & 0 & 0 \end{bmatrix} C/m^2$$

$$\varepsilon_{ij} = \begin{bmatrix} 44 & 0 & 0 \\ 0 & 38.75 & -7.27 \\ 0 & -7.27 & 34.65 \end{bmatrix}$$

Figure 5.4 $LiNbO_3$ Piezoelectric Matrices

5.3 Insertion Loss

Insertion loss is a widely-studied field in acoustics. Insertion loss in microfluidic devices can be attributed to two chief sources, intrinsic and extrinsic loss. Intrinsic loss is attributed to absorption from molecular vibrations in the piezoelectric substrate. These types of intrinsic losses are increased proportionally with the length of the delay line between both in the input and output IDTs as shown in Figure 5.5, as well as lesser effects from edge, side, and bottom losses. In this finite element analysis study, the attenuation of wave travel in the delay line path of the surface acoustic wave device will be the primary focus of insertion loss calculation and simulation. In addition to delay line loss, the locations of edge losses, side losses, and bottom losses are depicted in Figure 5.5.

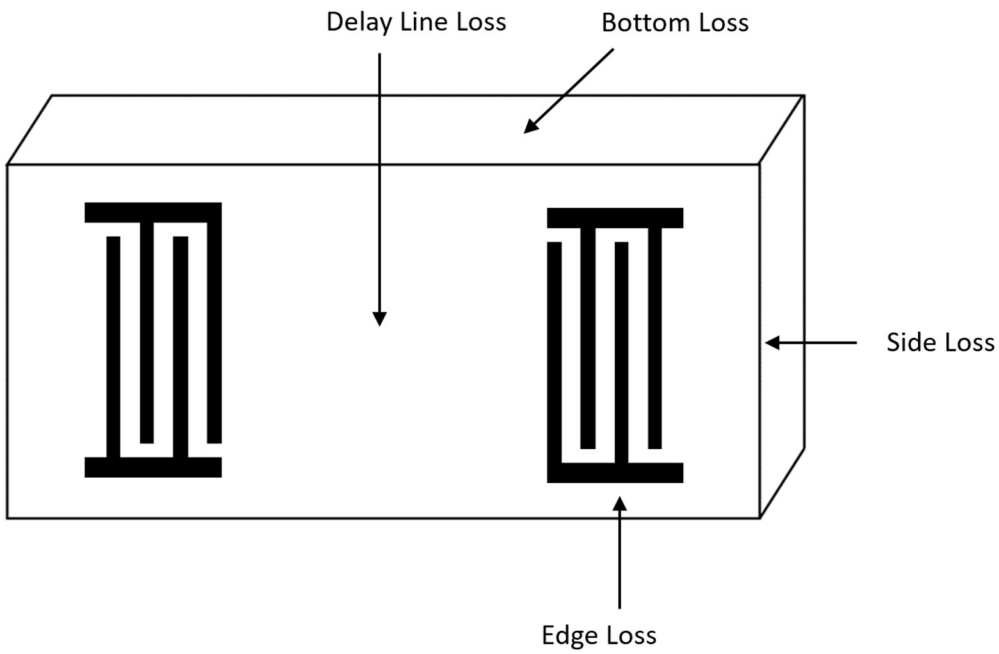

Figure 5.5 Delay Line, Edge, Size, and Bottom Losses

Extrinsic losses are caused by interaction of the piezoelectric substrate with foreign materials. This includes not only the PDMS channel placed on the wafer, but also the IDT fingers deposited on it. Although the IDT fingers are a cause of insertion loss, for this study, only the insertion loss from the PDMS is considered.

5.4 Meshing

Meshing is a critical aspect of any Finite Element Analysis. Three key points of meshing that need to be addressed in any simulation to ensure accuracy and efficiency of a solution are: mesh type method, mesh density, and mesh elements utilized.

The first aspect, mesh type method, refers to the selection between structured and unstructured mesh creation. In an unstructured mesh, number and density of mesh elements and nodes are decided arbitrarily by an FEA modelling package. Although this simplifies the process of mesh creation, it can lead to several errors and inaccuracies in results from creation of stress concentrations, and high aspect ratio elements. Aspect ratio is defined as the ratio of the length of

the longest side of a generated mesh element divided by the length of its shortest side. Elements with aspect ratios of greater than three are suspect, and with ratios of ten or greater are highly probable for non-convergence of simulated solutions. Figure 5.6 demonstrates two and three-dimensional mesh elements with favorable and non-favorable aspect ratios [58].

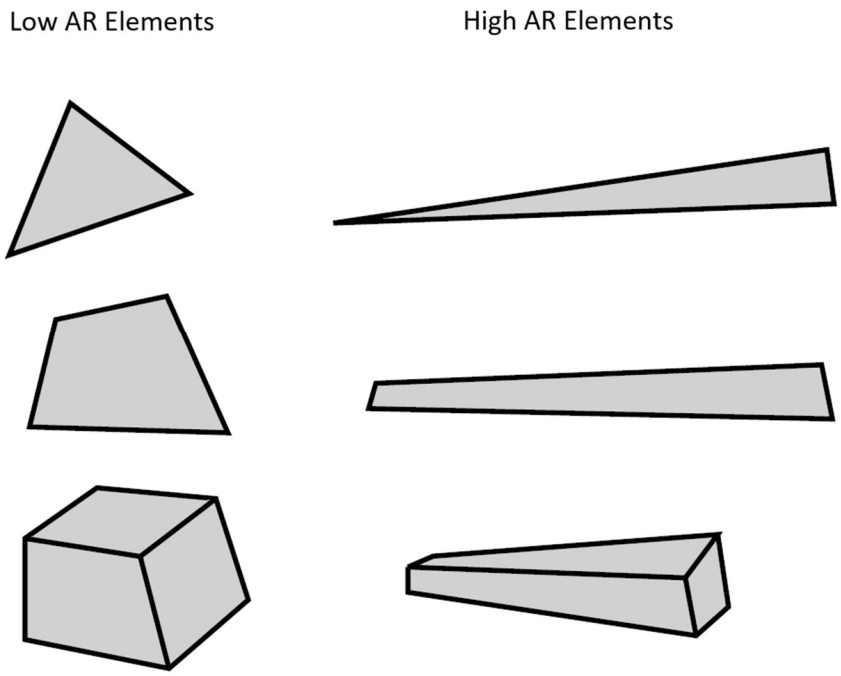

Figure 5.6 Low and High Aspect Ratio Elements [26]

A structured mesh allows the user complete control of the mesh generation process. This ensures high quality of elements generated, and control over the second aspect of meshing, mesh density.

The second aspect that must be considered is mesh density. Increasing mesh density minimizes the size of individual mesh elements, which increases the time needed for solution computation as well as the computing power necessary to calculate. For this reason, mesh density is sometimes used in a gradient, where the mesh density increases as the mesh approaches the area of interest of a model. If the growth rate of the mesh density is not carefully considered, higher

aspect ratio elements are generated. For this reason, in this simulation study, the mesh density is constant and defined by elements per wavelength. For acoustic analysis, six to ten elements per wavelength is recommended [22]. Constant mesh density also allows for the use of hexahedral, or brick elements.

The type of mesh elements used in simulation is dictated by the type of study being computed as well as the geometry being studied. Hexahedral elements are the preferable elements shape, but their use is limited in situations where a geometry is not easily divided into brick elements. Hexahedral elements provide higher accuracy of results when compared to the same number of tetrahedral elements, as a result of more nodal points per element. Tetrahedral and pyramid shaped elements are useful when increasing a mesh density close to the area of interest being studied; however, in this simulation study, a relatively thin substrate allows for the constant mesh density throughout its thickness. The simple shape of the piezoelectric substrate simulated also lends itself towards a hexahedral mesh.

5.5 Methods

The simulation study performed here was completed in multiple steps and was modeled after experimental results presented in a previous study [26]. The purpose was to compare the insertion loss of an arbitrary signal input across a piezoelectric substrate to varying side wall dimensions of a polydimethylsiloxane (PDMS) channel. All simulations were carried out via ANSYS® Workbench 15.0 Finite Element Analysis (FEA) software. The study was completed in series of six simulations. The first two simulations were calibration of a bare lithium niobate wafer's boundary conditions. The details of the first simulation geometry are illustrated in Figure 5.7 and Figure 5.8.

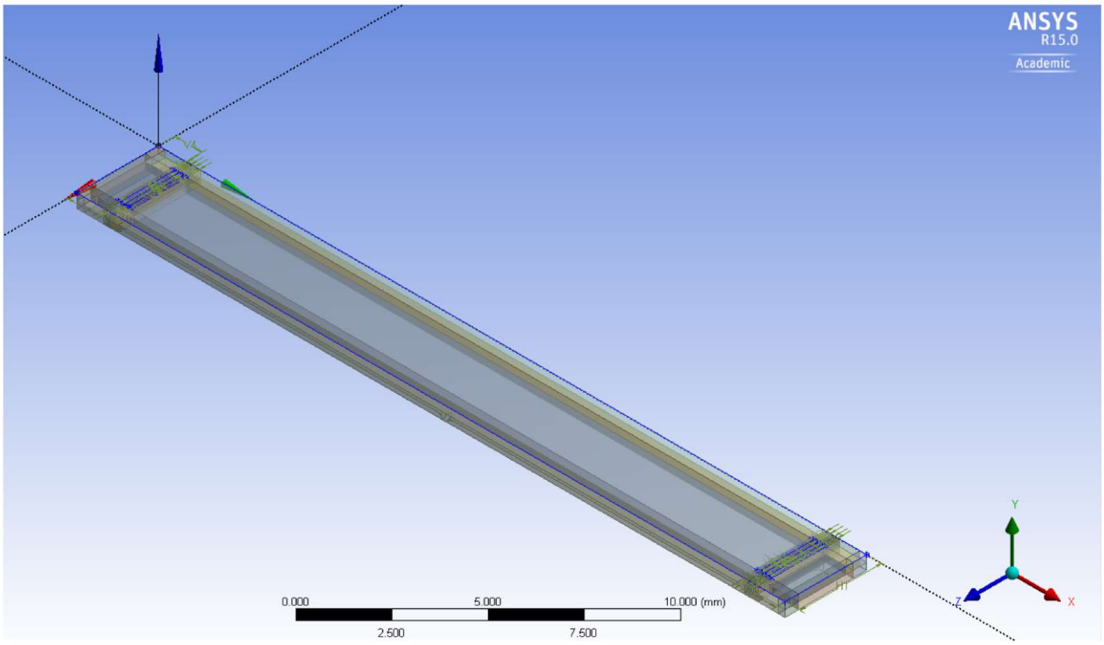

Figure 5.7 Square End Model Geometry

The lithium niobate (LiNbO3) wafer depicted in Figure 5.7 is 26 mm long in the *x*-axis direction, 3 mm wide in the *z*-axis direction, and extruded 0.5 mm thick in the *y*-axis direction. These are shown in Figure 5.8 as the length (*L*), width (*W*) and thickness (*T*), respectively. The orientations of SAW devices for different cuts are given in a number of publications[56, 59]. Slices were introduced into the geometry to allow for more consistent meshing control. After the slices were created, the geometry was then consolidated as one part consisting of 122 separate bodies. At either end of the wafer, there is one interdigital transducers (IDTs) which consists of four fingers that are 1 mm long (h), 0.075 mm wide (d), and are imprinted directly onto the face of the substrate [60-62]. The width of the IDTs was specified as one quarter of the 300-micrometer wavelength (*l*) simulated in the lithium niobate wafer. One of IDTs was meant as an input transducer, and the opposing IDT was utilized as a sensing set. The input set of fingers were excited with a pulse input, and the sensing fingers were responsible for capturing the signal transmitted across the wafer. The pulse input parameters are detailed in equation (31).

$$V_A = \begin{cases} +1V, & t \leq 1ns \\ 0V, & t > 1ns \end{cases} \tag{31}$$

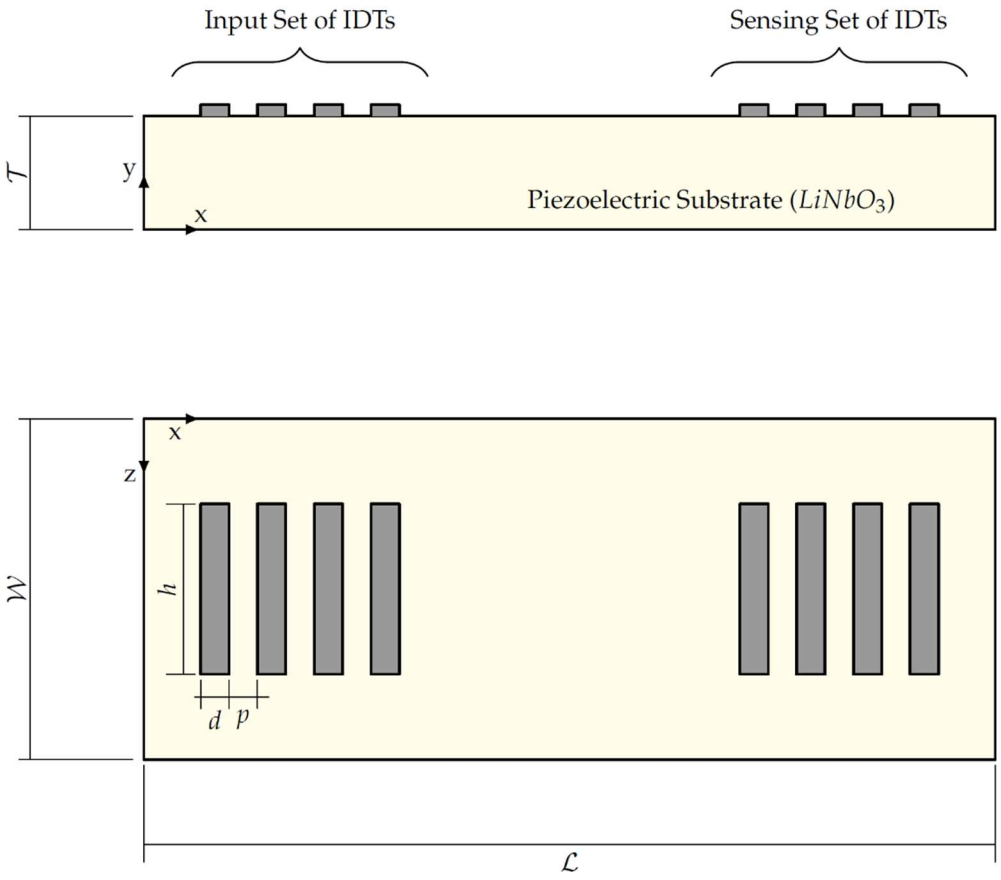

Figure 5.8 Schematic View of the SAW Device

Figure 5.11 illustrates the meshing as well as the location of the actuating IDTs. In this figure, the fingers labeled "A" were subjected to the voltage input loading condition in equation (31). The fingers not excited under this loading condition were in a constantly grounded state, so that two fingers were pulse inputs and two were constantly grounded, these grounded fingers are denoted as "B" in the figure. Similarly, at the opposing end of the substrate, the fingers alternate between IDTs used for sensing, and IDTs that were constantly grounded. The entire bottom face of the wafer had a fixed boundary condition.

The meshing parameters for this study were chosen in order to properly characterize surface waves excited. Figure 5.9 demonstrates hexahedral element type nodal point placements of the mesh type used in this simulation

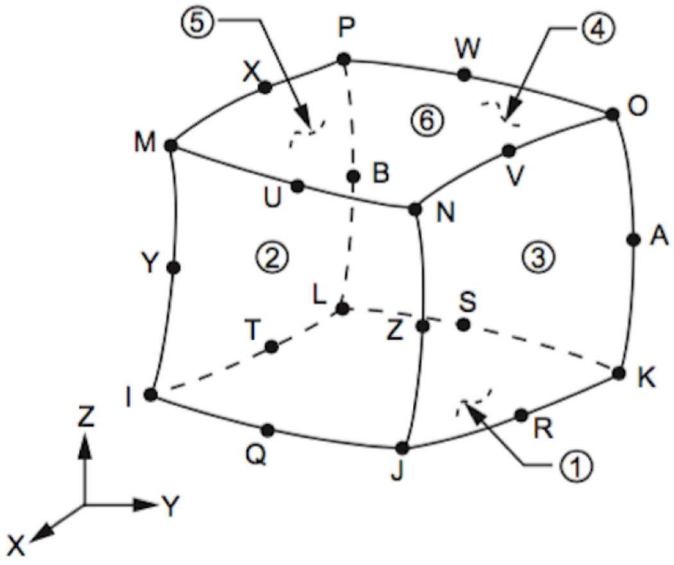

Figure 5.9 Three Dimensional 20 Node Hexahedral Element [26]

These mesh elements placed in the delay line path of the piezoelectric substrate had an edge length of 75 μm; furthermore, the piezoelectric element type has four degrees of freedom (DOF). Respectively these are three displacement DOF, as well as one electric DOF. As each hexahedral element contains three nodal points in the direction of wave propagation, nine total nodal points characterize the traveling wave, Figure 5.10 demonstrates this. Here A represents a surface wave, fixed at both ends, and B represents an undeformed substrate surface. Each nodal point is one point of motion on the traveling wave, that is propagating. If the density of nodal points along the wave is lower, there is not significant information per wavelength to properly characterize a traveling wave, conversely if the density is too high, then there is an abundance of nodal points that will increase computational power required, without significantly increasing result accuracy.

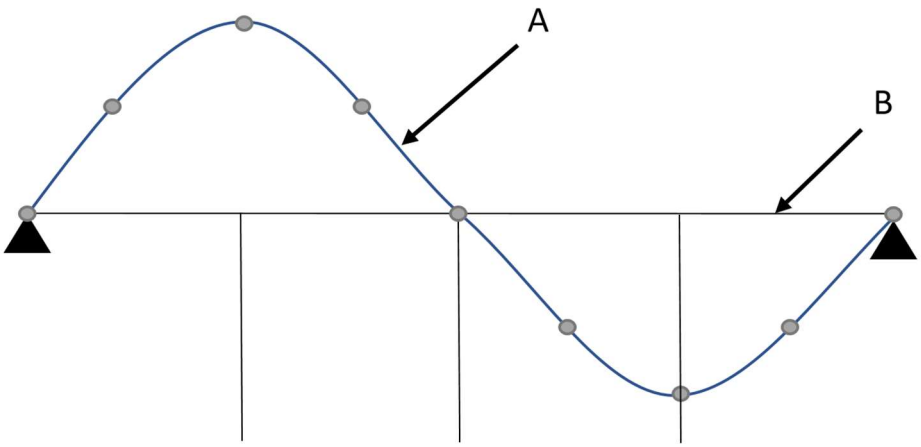

Figure 5.10 Surface Wave Propagation Characterized by 9 Nodal Points

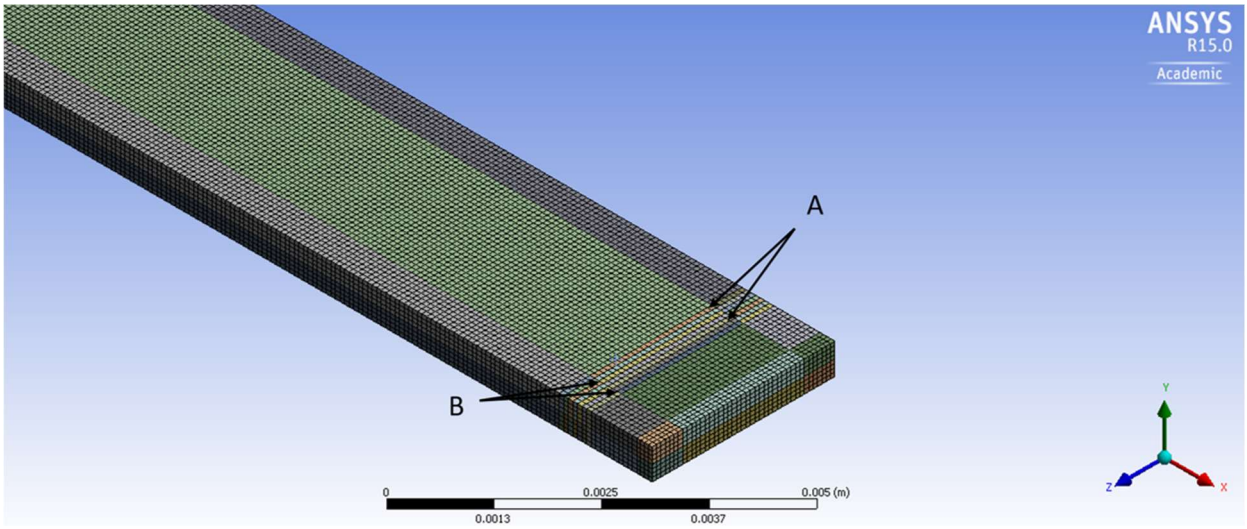

Figure 5.11 First Simulation Meshing and IDT Locations

Spatial discretization is a critical step in simulation, and the quality of a mesh can be analyzed in ANSYSR via mesh statistics. Three key statistics that were recorded in each simulation were the skewness, orthogonal quality, and element quality. The ANSYSR guide specifies that a skewness of less than 0.25 and on orthogonal quality of 0.95 are considered excellent [27]. The average values for skewness and orthogonal for the simulations completed in this study were 1.83×10^{-3} and 0.99, respectively. Element quality of greater than 0.3 is considered good quality,

the average element quality for the five simulations in this study was 0.989. Specifying the specific mesh types and sizing, as opposed to automatically generating meshes, allowed for creation of high quality mesh elements. Temporal discretization is equally as relevant to creating a proper simulated event as spatial discretization. To properly characterize a wave created on the piezoelectric substrate modeled, equation (32) is utilized.

$$T_v < \frac{1}{20 * f_{max}} \tag{32}$$

where T_v is the duration of each time step necessary to characterize a studied frequency of f_{max}. In the case of this simulation the f_{max} is found from the spacing of the IDT fingers, which gives a wavelength of 300 µm. The surface wave velocity of 128° Y-cut X-axis propagating $LiNbO_3$ substrate is given as 3980 m/s. Thus, the excitation frequency can be calculated as.

$$f = \frac{v}{\lambda} = \frac{3990\ m/s}{300\ \mu m} = 13.3\ MHz \tag{33}$$

This frequency requires a T_v of maximum 3.75 ns. This simulation exceeds that standard with time step durations of 3.33 ns.

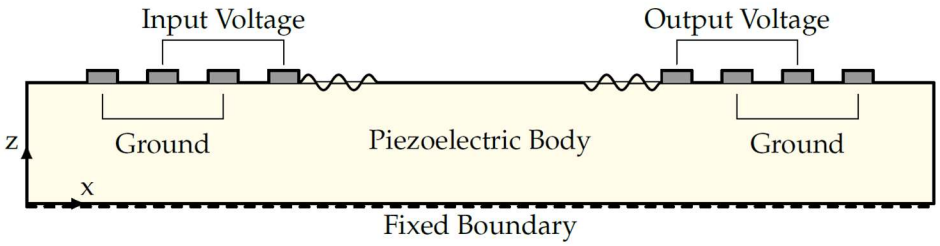

Figure 5.12 Boundary Conditions for the SAW Device

The first and second simulations completed in this study were both for bare lithium niobate wafers; however, the first simulation was completed for a substrate with a square end and the second was completed for a substrate with a rounded end. The first simulation results contained excessive noise from wave reflection at the square ends of the substrate. The use of rounded edges

to minimize reflection in simulating SAW devices has been shown to account for boundary reflection characteristics [28,29]. As illustrated in Figure 5.13, we employed the rounded edge wafer strategy to minimize the reflections from the edges. It should be highlighted that in experimental studies, the wafer is diced further away from the microfluidic transducer location, hence changing the substrate edge will not have significant impact in the application space. With the minimization of noise, peak operation frequency of the piezoelectric device can be more clearly determined through FFT analysis. These rounded ends are semicircular with a radius of 0.5 mm. All boundary conditions in this simulation were identical to the boundary conditions of the square end substrate.

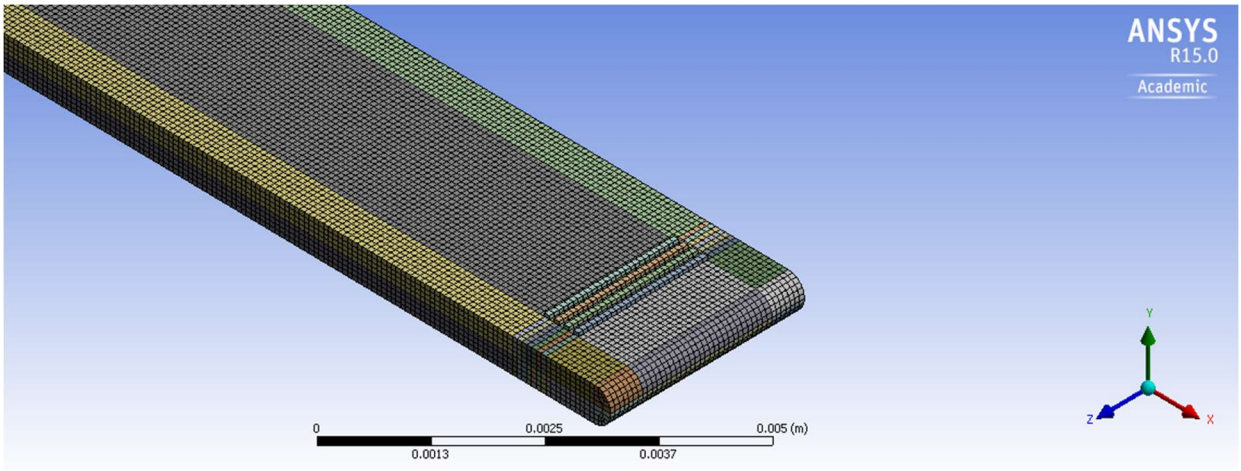

Figure 5.13 Improved Simulation with with Rounded End Substrate

After the rounded edge model was selected, PDMS channels were constructed on the top face of each substrate simulated, Figure 5.14. The PDMS was modeled as sylgard 184 with a density of 1.03 $\frac{kg}{m^3}$ and a Young's modulus of 1.32 MPa [63]. The PDMS channels were modeled with the same mesh density as the piezoelectric substrate. A total of four simulation variations were completed, with each containing a varying PDMS side wall channel thickness. These were then compared to the insertion loss of the bare lithium niobate wafer for relative insertion loss

differences, and then compared to experimental data to study the accuracy of the results. The PDMS side wall channels were simulated at eight millimeter, six millimeter, four millimeter, and two millimeter thicknesses. All varying simulations of the side wall thickness had a constant top wall thickness of eight millimeter. Each simulation was run with consistent boundary conditions and voltage inputs. For reference, geometries of each PDMS channel are shown in Figure 10. This figure overlays all four different channel dimensions. The PDMS channels were specified as a separate body from the actual piezoelectric substrate, and subsequently modeled with a "bonded" condition through the ANSYSR contact selection to the substrate. The bonded condition mimics the plasma etching that is used to bond PDMS channels to substrates during experimentation.

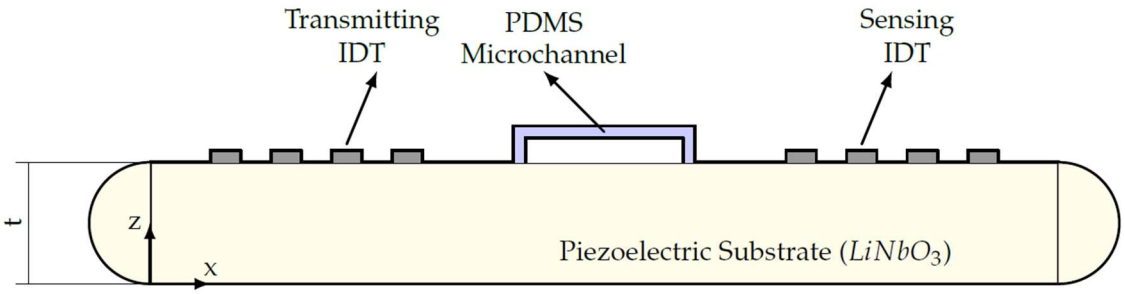

Figure 5.14 Schematic Side View of SAW Device with PDMS

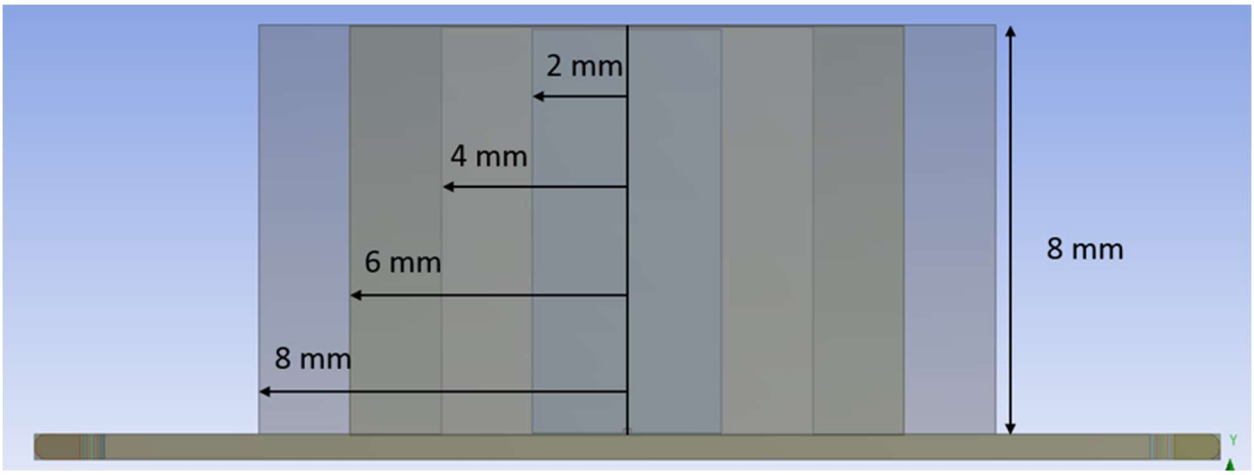

Figure 5.15 Side View of Varying PDMS Channel Dimensions

The insertion loss levels were calculated in dB through a custom MATLAB file, which utilized formula (34).

$$IL = 10\log_{10}\left(\frac{P_{out}}{P_{in}}\right) \tag{34}$$

The goal of this procedure was to determine the relative decibel (dB) drop directly associated with variation of the PDMS channel sidewall thickness. Figure 5.16 shows the components and boundary conditions of the simulations with PDMS channels, where A and B are the location of the input IDTs, and C is the PDMS channel.

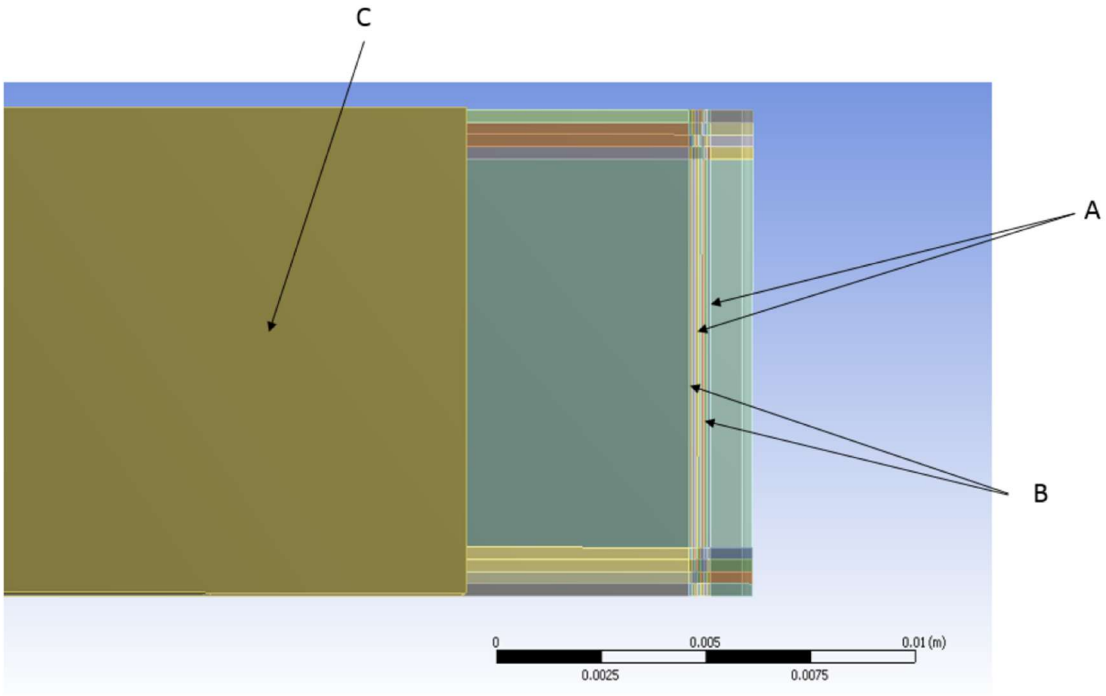

Figure 5.16 Top View of Substrate and Load IDTs

5.6 Results and Discussion

The results of the simulation show the total insertion loss of the bare lithium niobate substrate compared with the insertion losses of four PDMS channels at constant eight mm top wall thickness and four varying side wall thicknesses. In each simulation, the microfluidic channel

contains no liquid. These results are presented in Figure 5.17 and Figure 5.18. Figure 5.17 shows a frequency response spectrum from 7.7 MHz to 22 MHz. Figure 5.18 shows only the insertion loss for the operational frequency of the piezoelectric devices. The operation frequency peak found for all simulated cases was 13.3 MHz. The largest difference, 11.52 dB, in insertion loss exists between the bare wafer and wafer with eight mm side wall channel.

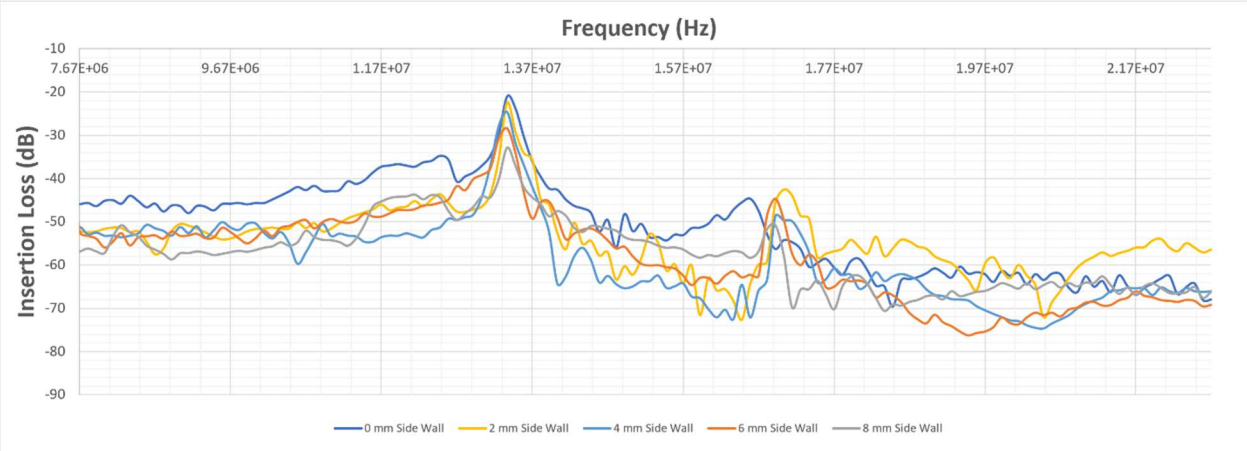

Figure 5.17 Insertion Loss Spectrums for Varying PDMS Channels

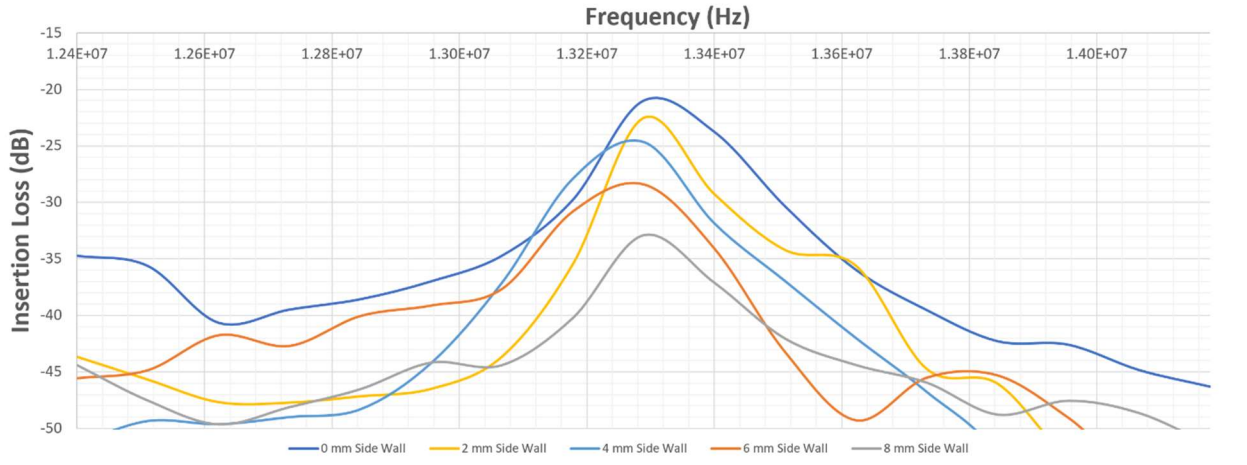

Figure 5.18 Insertion Loss for Varying PDMS Channels at Operation Frequency

Lastly, Table 5.2 compares the relative insertion losses calculated in simulation compared to experimental insertion losses at peak frequency responses for the piezoelectric substrates. The experimental data referenced in this comparison is from previously published work [64].

Table 5.2 Insertion Loss at Resonant *f* Relative to No Channel in Decibels

	Simulation Δ *IL*	Experimental Δ *IL*
8 mm	-11.52	-10.11
6 mm	-6.28	-6.58
4 mm	-4.41	-2.39
2 mm	-3.21	-0.82

For the results presented here, the effects of bulk acoustic wave action and electric field outside of the substrate are assumed to be negligible. The experimental versus simulated results show that as the PDMS channel side wall thicknesses increases, the relative insertion loss increases, which is expected. Also as the sidewall thickness is increased, the results between the simulated and experimental insertion loss converge. A paired t-test run between each individual IL levels calculated, shows that on average there is a p-value of 0.035, demonstrates statistically significant data. Any impedance in the delay line path of a piezo electric device will create an insertion loss; however, there is a nonlinear change in insertion loss levels found with varying side wall channel thicknesses. This nonlinear change can be attributed to the SAW interaction with the viscoelastic PDMS material. There is an exponential leakage of the SAW wave as it interacts with the surface of the PDMS, which dictates that the insertion loss levels of a given piezoelectric device is greatly improved by monitoring the PDMS channel dimensions. Although the thinnest side wall channel dimensions should be employed, it is shown by simulation, and confirmed by experimentation, that the relatively small difference between a two and four-millimeter side wall channel IL allows for flexibility of PDMS channel dimensions in that range.

The variation that does exist between the experimental and simulated data can be attributed to a few sources. Firstly, the simulated geometry was different than the experimented geometry. The largest geometry differences were the number of IDT fingers simulated, as well as the length of these fingers. Altering the scale of the simulated geometry to come closer to the experimental geometry exponentially increases both the time necessary for the simulation to complete, as well as the total computational power needed to run the simulation. Secondly, the relative dB loss values are calculated from the case where there is no PDMS channel on the substrate, this bare wafer is the zero dB baseline. Any changes in this baseline, experimentally or in the simulation, shifts the values of the insertion losses for the remaining four varying PDMS channels. Finally, error and variation in the original experimentation will affect how closely the simulated data matches the experimental data. In the simulation case, if all the boundary conditions and meshing parameters are mirrored, the results calculated are the same; however, with experimentation it is impossible to consistently acquire the exact same results. Repetition of the original experimentation will shift not only the baseline zero dB measurement, but also all of the PDMS channel insertion loss measurements. This consequently effects the matching of the experimental and simulated data. Furthermore, there is a nonlinear relationship between the power load applied to a piezoelectric device, and it's output electrical field created. This can also effect the total level of insertion loss calculated through simulation, as the voltage input in experimentation was much higher than the voltage input level simulated in this study.

5.7 Conclusion

In this study, the effect of varying PDMS channel side wall thicknesses on insertion loss of a $LiNbO_3$ substrate was simulated via ANSYS® Workbench 15.0 Finite Element Analysis software. The results show a clear trend of decreasing insertion loss levels, when compared to a

bare substrate, as the side wall thicknesses are varied from eight to two millimeters. The six-millimeter reduction of the simulated sidewall thickness resulted in a net decrease of 8.31 dB of insertion loss. These results further show that as the sidewall thickness increased, there was a converging of simulated and previously published experimental data. The ability to replicate experimental data through simulation, by rigorous attention to boundary conditions and input parameters, is a necessary step for creating trustworthy models that can be used for predictive analysis.

CHAPTER 6. CONCLUSIONS AND FUTURE WORK

6.1 Summary

This dissertation is comprised of work from two studies. The first is the calibration of an ultrasonic transducer, for use in bone conduction audiological studies. The second study is the simulation of insertion loss levels of a piezoelectric substrate with varying PDMS channels. Both studies find their roots in the field of acoustics.

In the first study, the calibration of an ultrasonic transducer, the free response of a transducer was compared with the calibration of the same transducer when placed under a static loading condition. This static loading condition mimicked the operation condition of the transducer in an audiological application. Previous studies have been performed for the same topic; however, these studies only aimed to calibrate the sound pressure levels of transducers being employed. These studies were more focused on the hearing perception of subjects that were exposed to these transducers. To this end, this dissertation created a novel method which compared the free response and statically loaded transducer. It was found that the static loading dampened the response of the transducer, but had the dual effect of broadening its response. This can be attributed to the static load modifying the at-rest conditions of the piezoelectric element in the transducer. Piezoelectric elements are characterized by mechanical and electrical stimuli causing shifts in their non-centrosymmetric crystalline structure. If the static condition of the piezo element is modified by the introduction of a load, it can be understood that its response to a stimulus would be similarly affected. For use in audiological purposes, this is a desired consequence of placing the transducer

under load. This allows for one transducer to be used for ultrasonic testing in a broader frequency spectrum.

The second study is simulation of insertion loss levels on varying PDMS channel side wall dimensions. This study was completed and compared to previously gathered and published experimental data. It was found that the simulated data experienced increased levels of insertion loss as the PDMS side wall channel thicknesses increased from two to eight millimeters. This was in agreement with the trend experienced in experimental data; furthermore, it was shown that as the simulated thicknesses of side wall channels were increased, there was a closer agreement between the two sets of data. The contribution of this portion of the dissertation was the bottom up creation of a reliable surface acoustic wave simulation in three dimensions. Simulated work to date regularly is done in two dimensions to simplify calculations, or often with prepackaged material library data for different piezoelectric substrates. Use of prepackaged material data is acceptable in most circumstances, however, it limits the user to a defined library of materials. When a piezoelectric crystal is cut in different planes and angle orientations, there is a shift in its properties. This creates the need to successfully recalculate its properties in order to properly simulate its response.

6.2 Future Work

The ultrasonic transducer calibration method includes gathering data on the amount of dampening that is experienced in transducer output in relation to the level of static load that is applied to its actuating face. With repeated experimentation of varying transducers, it can be determined if there is an equation that can relate these two variables within a certain level of accuracy. Further, improvements can be made on the stabilization rig that was created for the

calibration procedure. These improvements should eliminate any residual vibration created during calibration.

In the simulation study performed, future work will include creation of a coupled fluid flow and transient structure simulation. The fluid flow will be introduced with particle tracking in order to study the separation mechanics that take place inside the microfluidic channel as it is subjected to vibrations from the piezoelectric substrate. This result will then be compared to piezoelectric particle simulation experimental data already performed. The aim of further validation should be to create a simulation that can be used for the purposes of predictive analysis, rather than only study of already completed experimental work.

REFERENCES

1. Rayleigh, L., *On Waves Propagated along the Plane Surface of an Elastic Solid.* John Hopkins University Circulars, 1885. **4**(42): p. 4-11.

2. Nguyen, N.-T., *Droplet Microreactor*, in *Encyclopedia of Microfluidics and Nanofluidics*, D. Li, Editor. 2013, Springer US: Boston, MA. p. 1-7.

3. Wolfbeis, O.S., *Piezoelectric Sensors*. Sensors and Biosensors, ed. C.S. Andreas Janshoff. Vol. 5. 2007, Berlin Heidelberfg New York: Springer.

4. Sapna Tyagi, V.G.M., *SAW and Interdigital Transducers.* International Journal of Scientific & Engineering Research, 2012. **3**(12).

5. Chang, K., *RF and microwave wireless systems*. Wiley series in microwave and optical engineering. 2000, New York: Wiley.

6. Bhavikatti, S.S. and ProQuest, *Finite Element Analysis*. 1st ed. ed. 2004, Daryaganj: New Age International Pvt. Ltd., Publishers.

7. Corso, J.F., *Bone-Conduction Threshold for Sonic and Ultrasonic Frequency.* The Journal of the Acoustical Society of America, 1963. **35**(11).

8. Thomas M. Adams, R.A.L., *Introductory MEMS: fabrication and applications*. 2010, New York: Springer.

9. Cecile Malagrange, C.R., Michel Schlenker, *Symmetry and Physical Properties of Crystals*. 2011, Dordrecht Heidelberg New York London: Springer.

10. Newnham, R.E., *Perperties of Materials*. 2005, New York, NY: Oxford University Press.

11. Rose, J.L., *Ultrasonic waves in solid media*. 1999, Cambridge ; New York: Cambridge University Press.

12. Rushchit͡skiĭ, I.A.I.A.a., *Nonlinear elastic waves in materials*. Foundations of engineering mechanics. 2014, Cham: Springer.

13. Starmenclock. *A picture of a Rayleigh Wave*. 2006 http://www.geo.mtu.edu/UPSeis/rayleigh_web.jpg]; A Rayleigh wave / surface acoustic wave (SAW)].

14. Woudloper. *A Love wave*. 2007 [cited http://www.geo.mtu.edu/UPSeis/love_web.jpg.

15. Mason, W.P. and ProQuest, *Physical Acoustics V7 : Principles and Methods*. 2012, Saint Louis: Elsevier Science.

16. R.M. White, F.W.V., *Direct Piezoelectric Coupling to Surface Elastic Waves.* Applied Physics Letters, 1965. **7**(12).

17. Morgan, D. and ProQuest, *Surface Acoustic Wave Filters : With Applications to Electronic Communications and Signal Processing*. 2nd ed. ed. Studies in Electrical and Electronic Engineering. 2010, Kidlington: Elsevier Science.

18. Campbell, C. and ProQuest, *Surface Acoustic Wave Devices and Their Signal Processing Applications*. 2012, Saint Louis: Elsevier Science.

19. M. Jo, R.G., *Dual Surface Acoustic Wave-based Active mixing in a Microfluidic Channel.* Sensors, 2013. **196**: p. 1-7.

20. Zakaria, M.R., et al. *Fabrication and characterization of SAW IDT biosensor for biomolecule detection*. in *2015 IEEE Regional Symposium on Micro and Nanoelectronics (RSM)*. 2015.

21. Fish, J. and T. Belytschko, *A First Course in Finite Elements*. 2007, West Sussex PO19 8SQ, England: John Wiley & Sons Ltd.

22. Howard, C.Q.a. and B.S.a. Cazzolato, *Acoustic analyses using MATLAB® and ANSYS®.* 2015, Boca Raton: CRC Press.

23. Pidaparti, R.M. and ProQuest, *Engineering Finite Element Analysis*. 1st ed. ed. Synthesis Lectures on Mechanical Engineering. 2017, San Rafael: Morgan & Claypool Publishers.

24. Javidinejad, A., *FEA Practical Illustration of Mesh-Quality-Results Differences between Structured and Unstructured Mesh.* International Scholarly Research Network, 2012. **2012**.

25. Madenci, E.a. and I.a. Guven, *The finite element method and applications in engineering using ANSYS®.* Second edition. ed. 2015, New York: Springer.

26. *ANSYS Inc, ANSYS® Academic Research, Release 15.0, Meshing User's Guide*. 2013.

27. Apel, T. and O. Steinbach, *Advanced finite element methods and applications*. Lecture Notes in Applied and Computational Mechanics ; 66. 2010, Dordrecht: Springer.

28. Marks, R.J. and ProQuest, *Handbook of Fourier Analysis & Its Applications*. 2009, New York: Oxford University Press, USA.

29. Martin L. Lenhardt, R.S., Peter Wang, Alex M. Clark, *Ultrasonic Speech Perception.* Science, 1991. **253**(5015): p. 82-85.

30. Gavreau, V., *Pneumatic Generators of Intense Ultrasound.* Journal of the Acoustical Society of America, 1956. **28**(4): p. 803.

31. Pumphrey, R.J., *Upper limit frequency for human hearing.* Nature, 1950. **166**: p. 166.

32. Kollmeier, B., *Hearing, from sensory processing to perception*. 2007, Berlin, NY: Springer.

33. College, O., *Anatomy & physiology*. 2013, OpenStax CNX: Houston, TX. p. Retrieved from http://cnx.org/content/col11496/latest/.

34. staff, B.c., *Medical gallery of Blausen Medical 2014*, W.o.M. 1, Editor. 2014.

35. L.E. Dreisbach, J.H.S., *Distortion-product otoacoustic emissions measures at high frequences in humans.* Journal of the Acoustical Society of America, 2001. **110**(5): p. 2456-2469.

36. Lenhardt, M.L., *Ultrasonic Hearing in Humans: Applications for Tinnitus Treatment.* International Tinnitus Journal, 2003. **9**(2).

37. Tadashi Nishimura, S.N., Takefumi Sakaguchi, Hiroshi Hosoi, *Ultrasonic masker clarifies ultrasonic perception in man.* Hearing Research, 2003. **175**: p. 171-177.

38. Dan Yang, B.X., Xu Wang, Xueqin Jia, *The Study of Digital Ultrasonic Bone Conduction Hearing Device*, in *Engineering in Medicine and Biology 27th Annual Conference*. 2005: Shanghai, China.

39. Toshizo Koizumi, T.N., Akinori Yamashita, Toahiaki Yamanaka, Tomoaki Imamura, Hiroshi Hosoi *Residual Inhibition of tinnitus induced by 30-kHz bone-conducted ultrasound.* Hearing Research, 2014. **in press**.

40. Dunn, W. and ProQuest, *Introduction to Instrumentation, Sensors, and Process Control*. 2005, Norwood: Artech House.

41. R.H. Tancrell, M.G.H., *Acoustic Wave Filters.* IEEE, 1971 **59**(3): p. 393-409.

42. Campbell, C., *Surface Acoustic Wave Devices for Mobile and Wireless Communications*. 1998, London, UK: Academic Press Inc.

43. H. Wohltjen, R.D., *Surface Acoustic Wave Probe for Chemical Analysis Introduction and Instrument Description.* Anal. Chem, 1979. **51**(9): p. 1458-1464.

44. A.C. Stevenson, M.H.M., R.S. Sethi, L.E. Cheran, M. Thompson, L. Davies, C.R. Lowe, *Gigahertz surfae acoustic wave probe for chemical analysis.* Analyst, 2001. **126**: p. 1619-1624.

45. Tao Wang, Q.N., Nathan Crane, Rasim Guldiken, *Surface Acoustic Wave based Pumping in a Microchannel.* Microsystems. **in press**.

46. Tao Wang, R.G., R.R. Nair, Mark Howell, Subra Mohapatra, , *Surface Acoustic Waves (SAW)-Based Biosensing for Quantification of Cell Growth in 2D and 3D Cultures.* Sensors, 2015(15): p. 32045-32055.

47. M. Jo, R.G., *Particle Manipulation by Phase-shifting of Surface Acoustic Waves.* Sensors, 2014. **207**: p. 39-42.

48. N.B. Crane, O.O., J Carballo, Qi Ni, R. Guldiken, *Fluidic Assembly at the Microscale: Progress and Prospects.* Microfluid Nanofluid, 2013. **14**: p. 383-419.

49. M. Jo, R.G., *Active Density-based Separation using Standing Surface Acoustic Wves.* Sensors and Actuators, 2012. **187**: p. 22-28.

50. O. Onen, A.S., N. Gallant, P. Kruk, R. Guldiken, *Urinary Bcl-2 Surface Acoustic Wave Biosnesor for Early Ovarian Cancer Detection.* Sensors, 2012. **12**: p. 7423-7437.

51. R. Guldiken, M.C.J., N.D. Gallant, U. Demirci, J. Zhe, *Sheathless Size-based Acoustic Particle Separation.* Sensors, 2012. **12**: p. 905-922.

52. D. Fall, M.D., M. Ouaftouh, B. Piwakowski, F. Jenot, *Modelling based on Spatial Impulse Response model for optimization of InterDigital Transducers (SAW sensors) for Non Destructive Testing.* Physics Procedia, 2015. **70**: p. 111-112, 213-218.

53. OpenStax, A.P.O.C.M., 2016 http://cnx.org/contents/14fb4ad7-39a1-4eee-ab6e-3ef2482e3e22@8.25.

54. M.Z. Atashbar, B.J.B., M. Simpeh, S. Krishnamurthy *3D FE simulation of H_2 SAW gas sensor* Sensors and Actuators, 2005. **111-112**: p. 213-218.

55. G. Xu, Q.J., *A Finite Element Analysis of Second Order Effects on the Frequency Response of a SAW device.* Journal of Intelligent Material Systems and Structures 2001. **12**(2): p. 69-77.

56. Abdollahi, A., *Evaluation on Mass Sensitivity of SAW Sensors for Different Piezoelectric Materials Using Finite-Element Analysis.* IEEE Transactions on Ultrasonics, Ferroelectrics, and Frequency Control, 2007. **54**(12): p. 2446-2454.

57. Auld, B.A., *Acoustic fields and waves in solids*. Vol. 1-2. 1973, New York, NY: Wiley.

58. Dow, J.A.T., J.A.T. Dow, and ProQuest, *A Unified Approach to the Finite Element Method and Error Analysis Procedures*. 1st ed. ed. 1998, Burlington: Elsevier Science.

59. Ajay C. Tikka, S.F.A.-S., Derek Abbott, *Finite Element Analysis of a 3-Dimensional Acoustic Wave Correlator Response for Variable Acoustic Modes.* Modeling , Signal Processing, and Control for Smart Structures, 2008. **6926**.

60. Mohammed M. EL Gowini, W.A.M., *A Finite Element Model of a MEMS-based Surface Acoustic Wave Hydrogen Sensor.* Sensors, 2010. **10**: p. 1232-1250.

61. Zhang, G., *Nanostructure-Enhanced Surface Acoustic Waves Biosensor and Its Computational Modeling.* Journal of Sensors, 2009. **2009**.

62. K M Mohibul Kabir, G.I.M., YIlas M Sabri, Salvy P Russo, Samuel J Ippolito, Surech K Bhargava, *Development and experimental verification of a finite element method for accurate analysis of a surface acoustic wave device.* Smart Materials and Structures, 2016. **25**.

63. I D Johnston, D.K.M., C K L Tan, M C Tracey, *Mechanical characterization of bulk Sylgard 184 for microfluidics and microengineering* Journal of Micromechanics and Microengineering, 2014. **24**(035017).

64. Jo, M.C. and R. Guldiken, *Effects of polydimethylsiloxane (PDMS) microchannels on surface acoustic wave-based microfluidic devices.* Microelectronic Engineering, 2014. **113**: p. 98-104.